

Azimuthal Spoke Propagation in Hall Effect Thrusters

IEPC-2013-143

*Presented at the 33rd International Electric Propulsion Conference,
The George Washington University, Washington, D.C., USA
October 6–10, 2013*

Michael J. Sekerak* Benjamin W. Longmier[†] and Alec D. Gallimore[‡]
University of Michigan, Ann Arbor, MI, 48109

Daniel L. Brown[§]
U.S. Air Force Research Laboratory, Edwards Air Force Base, California 93524

and

Richard R. Hofer[¶] and James E. Polk^{||}
Jet Propulsion Laboratory, California Institute of Technology, Pasadena, CA 91109

Spokes are azimuthally propagating perturbations in the plasma discharge of Hall Effect Thrusters (HETs) that travel in the $E \times B$ direction. The mechanisms for spoke formation are unknown, but their presence has been associated with improved thruster performance motivating a detailed investigation. The propagation of azimuthal spokes are investigated in a 6 kW HET using high-speed imaging and azimuthally spaced probes. The spoke velocity is determined from high-speed image analysis using three methods with similar results. The spoke velocity for three discharge voltages (300, 400 and 450 V) and three anode mass flow rates (14.7, 19.5 and 25.2 mg/s) are between 1500 and 2200 m/s across a range of magnetic field settings. The spoke velocity is inversely dependent on magnetic field strength for lower B-fields and asymptotes at higher B-fields where a different oscillatory mode is noted in the thruster. An empirically approximated dispersion relation of $\omega^\alpha = v_{ch}^\alpha k_\theta^\alpha - \omega_{ch}^\alpha$ where $\alpha \geq 1$ yields a characteristic velocity that matches the ion acoustic speed for ~ 5 eV electrons which exist in the near-anode and near-field plume regions of the discharge. Dispersion plots from ion saturation reference probes in the plume 1.5 mean discharge channel radii downstream are qualitatively similar to high-speed imaging dispersion plots of the discharge channel. Spoke velocities calculated from the probes are consistently higher by 30 % or more. The measured spoke velocities and oscillation frequencies are compared to standard drifts and plasma waves such as $E \times B$ drift, electrostatic ion cyclotron, magnetosonic and various drift waves calculated from plasma properties internal to the discharge channel.

*Doctoral Candidate, Plasmadynamics and Electric Propulsion Laboratory, Department of Aerospace Engineering, 1919 Green Road, B107, Ann Arbor, MI 48105, msekerak@umich.edu

[†]Assistant Professor, Plasmadynamics and Electric Propulsion Laboratory, Department of Aerospace Engineering, 1320 Beal Avenue, Ann Arbor, MI, 48109, longmier@umich.edu

[‡]Arthur F. Thurnau Professor and Director, Plasmadynamics and Electric Propulsion Laboratory, Department of Aerospace Engineering, College of Engineering, 1320 Beal Avenue, Ann Arbor, MI, 48109, alec.gallimore@umich.edu

[§]Research Scientist, Aerospace Systems Directorate, In-Space Propulsion Branch, Air Force Research Laboratory, 1 Ara Rd, Edwards AFB, CA, daniel.brown@edwards.af.mil

[¶]Senior Engineer, Electric Propulsion Group, 4800 Oak Grove Dr., MS 125-109, Pasadena, CA, 91109, richard.r.hofer@jpl.nasa.gov

^{||}Principal Engineer; Propulsion and Materials Engineering Section, 4800 Oak Grove Dr., MS 125-109, Pasadena, CA, 91109, james.e.polk@jpl.nasa.gov

Nomenclature

A_0	= amplitude for Lorentzian fit, arb. units Hz^{-1}
B	= magnetic field, T
B_r/B_r^*	= normalized magnetic field
c	= speed of light, m s^{-1}
$c_{1,2}$	= linear fit coefficients
E	= electric field, V m^{-1}
f	= frequency, Hz
f_c	= camera frame rate, frames s^{-1}
f_m	= peak frequency for spoke order m , Hz
f_0	= center frequency for Lorentzian fit, Hz
$I_{IM,OM}$	= inner, outer magnet coil current, A
j	= discharge current density, A cm^{-1}
k_θ	= azimuthal wave number, rad m^{-1}
L_{chnl}	= discharge channel length, m
L_{pr}	= probe spacing, m
$L_{\nabla\varrho}$	= gradient length scale for parameter ϱ , m
m	= spoke order
m_{min}	= minimum spoke order
$m_{i,e}$	= ion, electron mass, kg
N_{bins}	= number of bins
N_{fr}	= number of frames
n	= plasma density, m^{-3}
$n_{i,e}$	= ion, electron density, m^{-3}
n_n	= neutral density, m^{-3}
PSD	= power spectral density, arb. units Hz^{-1}
q	= elementary charge, C
R_{chnl}	= mean discharge channel radius, m
R_{jk}	= linear cross-correlation between b_j and b_k
r	= radial location, m
T_e	= electron temperature, eV
t_d	= probe time delay, s
$t_{j,k}$	= time delay from bin n to m , s
V_p	= plasma potential, V
v_A	= Alfvén speed, m s^{-1}
v_{ch}	= characteristic velocity, m s^{-1}
v_{gr}	= group velocity, m s^{-1}
v_{ph}	= phase velocity, m s^{-1}
v_s	= ion acoustic velocity, m s^{-1}
v_{sp}	= spoke velocity, m s^{-1}
$v_{spj,k}$	= spoke velocity from bin n to m , m s^{-1}
v_{the}	= electron thermal velocity, m s^{-1}
v_θ	= azimuthal velocity, m s^{-1}
w_m	= weighting for spoke order m
z	= axial location, m
α	= dispersion relation power dependence
β	= spoke velocity to B_r/B_r^* power dependence
Γ	= full-width at half maximum for Lorentzian fit, Hz
ϵ_0	= permittivity of free space, F m^{-1}

η	= plasma resistivity, Ω m
$\Delta\theta_{j,k}$	= angular difference from bin n to m, deg
$\dot{\theta}_{sp}$	= spoke angular velocity, deg s ⁻¹
λ	= wavelength, m
μ_0	= permeability of free space, H m ⁻¹
σ_x	= standard deviation or standard error of variable x , units of x
τ_s	= shutter period, s
ϕ_{pr}	= probe phase lag, rad
Ω_e	= electron Hall parameter, rad s ⁻¹
ω	= frequency, rad s ⁻¹
ω_{ch}	= characteristic frequency, rad s ⁻¹
$\omega_{ci,e}$	= ion, electron cyclotron frequency, rad s ⁻¹
ω_{lh}	= lower hybrid frequency, rad s ⁻¹
$\omega_{pi,e}$	= ion, electron plasma frequency, rad s ⁻¹

I. Introduction

Spokes were first observed in Hall Effect Thruster (HET) type devices by Janes and Lowder¹ and they were identified as a possible mechanism for cross-field transport. Research on a Cylindrical Hall Thruster (CHT)^{2,3} showed that up to half of the discharge current can pass through a spoke. It was also reported that the CHT performance (measured by discharge current) increased when the spoke was not present.⁴ This can lead one to conclude that spokes are detrimental to HET performance. However, the annular device studied by Janes and Lowder differed from modern HETs and the CHT has a significantly different magnetic field topology and physical geometry (no inner wall); so direct comparisons may not be appropriate with those systems to modern annular HETs such as the SPT-100 and H6.

Research by Brown⁵ and McDonald⁶ on low voltage operation showed that thruster performance was increased when spokes were stronger in the H6. Recent results by Sekerak⁷ on mode transitions clearly shows that spoke behavior was dominant in so-called “local oscillation mode” where the thruster exhibited lower mean discharge current and discharge current oscillation amplitude. The H6 thrust-to-power is maximum when the thruster is operating in local mode with spokes clearly propagating and no significant breathing mode. Ref. 7 raises the causality question of whether spokes are responsible for the improved thruster performance or are indicators when the thruster is running optimally. Regardless, the association of spokes with improved thruster performance in the H6 drives us to understand the fundamental mechanisms of spoke mechanics in order to improve thruster operation.

This paper is organized as follows. Section II reviews the experimental setup and findings of the recent investigation into mode transitions that were intentionally induced by varying magnetic field. Section III describes different methods for calculating azimuthal spoke velocity and shows how the spoke velocities vary with magnetic field strength using the data acquired from the mode transition investigation. Section IV identifies possible mechanisms for spoke formation and investigates different drifts and plasma oscillations that may be responsible for azimuthal spokes. Section V discusses the possible implications of observed spokes, a different mode of plasma oscillations spoke velocity and wall effects on spoke propagation. Section VI summarizes the results of three different methods used to calculate spoke velocity with the correlation method as the preferred technique. Across a range of normalized magnetic field settings, the spoke velocity is 1500-2200 m/s for all operating conditions. The spoke velocity is inversely dependent on magnetic field strength for lower B-fields and asymptotes at higher B-fields where a different oscillatory mode is noted in the thruster. An empirically approximated dispersion relation of $\omega^\alpha = v_{ch}^\alpha k_\theta^\alpha - \omega_{ch}^\alpha$ where $\alpha \geq 1$ yields a characteristic velocity that matches the ion acoustic speed for ~ 5 eV electrons which have been measured in the near-anode and near-field plume regions of the discharge channel. Several different mechanisms and plasma waves are considered for spoke propagation with work continuing to identify the most likely mechanism.

II. Review of Mode Transition Oscillations

This section reviews a recent investigation into mode transitions in HETs that were intentionally induced by varying magnetic field strength.⁷ The high-speed imaging results and probe data from this experiment are used in Section III to develop methods for calculating azimuthal spoke velocity and determine how spoke velocity varies with magnetic field strength.

HETs have been under development for over 50 years with significant experimental and flight histories⁸ and mode transitions have been commonly observed throughout their development as noted by some of the early pioneering Russian research.⁹ HETs have several parameters that define a single operating point such as discharge voltage, magnetic field strength (or magnet coil current), anode mass flow rate and cathode mass flow rate. Laboratory HET discharge power supplies operate in voltage regulated mode where the discharge voltage between the anode and cathode is held constant and the discharge current is allowed to fluctuate. A general, qualitative description of mode transition can be deduced from previous research as the point while varying one parameter and maintaining all others constant, a sharp discontinuity is observed in the discharge current mean and oscillation amplitude. In one mode, the discharge current oscillation amplitude is small with respect to the mean discharge current value, while after the mode transition the mean discharge current rises sharply as well as the oscillation amplitude. Previous researchers have identified mode transitions in HETs^{5,9,10} where a small change in a thruster operating parameter such as discharge voltage, magnetic field or mass flow rates causes the thruster discharge current mean and oscillation amplitude to increase significantly and decrease thruster performance.⁷ Thrust-to-power is maximized in the mode where azimuthal spokes are present and begins to decrease by up to 25% when absent. Although spokes are not identified as the cause of the increased performance, their association suggests that investigating the underlying mechanism of spokes will benefit thruster operation.

A. Thruster and Facilities

A recent experiment induced mode transitions in a 6 kW class laboratory HET called the H6 shown in Fig. 1. The experimental setup is described in detail in Ref. 7 and only pertinent details are repeated here. The investigation was conducted in the Large Vacuum Test Facility (LVTF) of the Plasmadynamics and Electric Propulsion Laboratory (PEPL) at the University of Michigan. The test matrix included variations in discharge voltage and xenon propellant flow rates. Propellant mass flow rates tested were 25.2, 19.5 and 14.7 mg/s through the anode and 1.8, 1.4 and 1.0 mg/s (7% cathode flow fraction) through the LaB₆ cathode. Discharge voltages of 300, 400 and 450 V were applied between the anode and cathode. The xenon corrected chamber pressures were 8.5×10^{-6} , 1.1×10^{-5} and 1.4×10^{-5} Torr for 14.7, 19.5 and 25.2 mg/s anode flow rate, respectively. These pressures were measured with an external ionization gauge and differ from the previously reported pressures⁷ that were measured with a nude ionization gauge. Both of these gauges are mounted at the top of LVTF above the thruster (~ 3 m away) and the pressure measurement uncertainty was estimated to be 20%.¹¹ A more complete discussion of pressure measurements and pressure effects on HET operation is provided by Walker.¹²

The H6 was a joint development effort of the University of Michigan, the Air Force Research Laboratory (AFRL) at Edwards AFB, and the NASA Jet Propulsion Laboratory (JPL); a separate copy of the thruster is maintained at each institution. It is notable for its high total efficiency; e.g., 64% at 300-V (6-kW) with a specific impulse of 1950 s and 70% at 800-V (6-kW) with a specific impulse of 3170 s.¹³ Since first firing in 2006, the H6 has been well characterized by a variety of diagnostic and modeling techniques at Michigan,

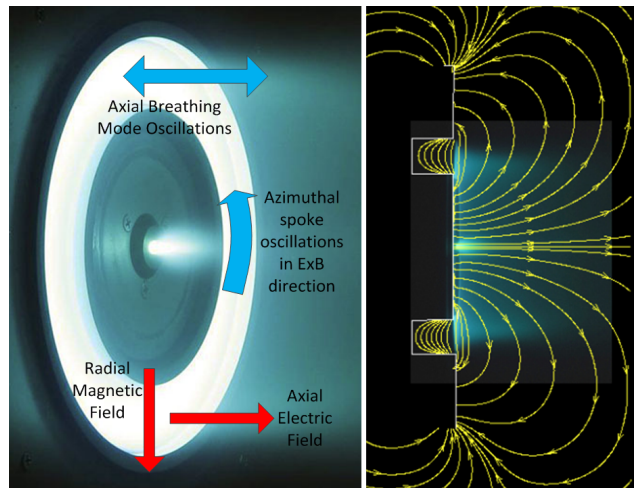


Figure 1: (Left) H6 with direction of magnetic field and $E \times B$ shown. (Right) Profile picture of the H6 operating at nominal conditions with magnetic field stream lines overlaid and discharge channel outlined. Reproduced from Figure 6 of Ref. 7.

AFRL and JPL. Six experimental doctoral dissertations have focused on the thruster to date, which have spawned numerous associated conference and journal articles.

The magnetic field shape shown in Fig. 1 was kept constant during testing, though the magnitude, noted by B_r/B_r^* , was varied throughout the testing in order to induce a mode change within the H6. The quantity B_r/B_r^* is the maximum radial magnetic field value at a particular setting of inner magnet (I_{IM}) current and outer magnet (I_{OM}) current divided by the nominal maximum radial magnetic field. The nominal magnetic field (B_r^*) strength (i.e., for maximum thruster performance) at 300 V and 20 A discharge current is $I_{IM} = 3.50$ A and $I_{OM} = 3.13$ A.¹³

B. FastCam and ISR Probes

High-speed imaging was acquired with a Photron SA5 FASTCAM with a Nikon ED AF Nikkor 80-200 mm lens at its maximum aperture f/2.8. The SA5 is capable of up to 1,000,000 fps with 128×16 pixel resolution, but was used at 87,500 fps with 256×256 pixel resolution for this testing. The camera was 6 m downstream from the thruster outside LVTF with a view of the thruster through a viewport. Details of the McDonald technique are given in Refs. 14 and 7, but a brief summary is provided here. The video is imported into MathWorks MatLab where each frame is a 256×256 matrix of light intensity values and the AC component is subtracted individually from each pixel. The discharge channel is isolated and divided into 180 two-degree bins. The pixels in each bin are averaged together generating a 180×1 vector of light intensity for each frame. A 2-D plot of all frames is the spoke surface where the ordinate is azimuthal location around the discharge channel in clock positions and the abscissa is time with each vertical column of values representing one frame of video. Adding all bins together yields the $m = 0$ or m_0 mode and was first shown by Lobbia¹⁵ to linearly correlate to the discharge current. During the mode transition investigation of Ref. 7 the same strong, linear correlation was also observed and used as the basis for converting light intensity to discharge current density with several assumptions.

The spoke surface or discharge current density surface yields valuable information on plasma oscillations within the discharge channel by showing the time-resolved, azimuthal distribution of light intensity. Vertical features represent extremes in discharge current density that occur everywhere in the channel simultaneously. Diagonal features are perturbations in discharge current density that propagate azimuthally around the discharge channel. Lines from upper-left to lower-right are propagating counter-clockwise around the discharge channel and lines from the lower-left to upper-right are propagating clockwise. The $E \times B$ direction in the H6 is counter-clockwise since the B-field direction is radially out. It was shown that all azimuthally propagating features are in that direction represented by lines from upper-left to lower-right with the slope corresponding to propagation velocity in deg/s. The High-speed Image Analysis (HIA) and two-dimensional Power Spectral Density (PSD) are discussed further in Section III.C.

Ion saturation reference (ISR) probes were positioned 1.5 discharge channel mean radii downstream at the 6 o'clock position on thruster center line as shown in Figure 9 of Ref. 7. The ISR probe gap was 29.5 ± 0.5 mm apart, which corresponds to $21.4^\circ \pm 1.7^\circ$ of azimuthal spacing; i.e., $\sim 11^\circ$ on either side of 6 o'clock. The probes were 0.13 mm diameter pure tungsten wire with 3 mm exposed. The ISR probes were biased to -30 V with respect to ground, which is more than 16 Te below the plasma potential and therefore are safely in ion saturation. The ISR current is measured external to the LVTF across a 100 Ω shunt resistor through an Analog Devices AD 215 120-kHz low-distortion isolation amplifier. The data acquisition system used to record discharge current and the ISR signals are sampled at rates up to 180 MHz with 16-bit AlazarTech ATS9462 digitizers.

C. Transition Results

The magnetic field B_r/B_r^* was varied by changing the inner and outer magnet coil currents in a constant ratio with all other parameters held constant including flow rates, discharge voltage, and chamber pressure. Maintaining a constant 1.12 ratio of inner to outer coil current allowed the magnetic field magnitude to be varied without changing the shape shown in Fig. 1. Decreasing B_r/B_r^* below a certain threshold was shown to repeatedly induce a mode transition where the mean discharge current increased and the discharge current amplitude increased. An example of this transition is shown at the top of Fig. 2. The mean discharge current and oscillation amplitude (Root-Mean-Square or RMS) are lowest in local mode ($B_r/B_r^* > 0.61$) and then increase sharply in global mode ($B_r/B_r^* < 0.61$). The transition point is $B_r/B_r^*|_{trans} = 0.61$. A defined transition B_r/B_r^* is misleading because there is a transition region where the plasma exhibits both types of

oscillations as shown in Fig. 2, however the transition typically occurred over only $\sim 10\%$ change in B_r/B_r^* . Figures 12, 13 and 14 of Ref. 7 shows that $B_r/B_r^*|_{trans}$ increases with increasing flow rate and discharge voltage. The spokes shown in Fig. 2 for $B_r/B_r^* = 1.00$ and 1.48 are localized oscillations that are typically 10-20% of the mean discharge current density value, while the oscillations in global mode $B_r/B_r^* = 0.52$ can be 100% of the mean value.

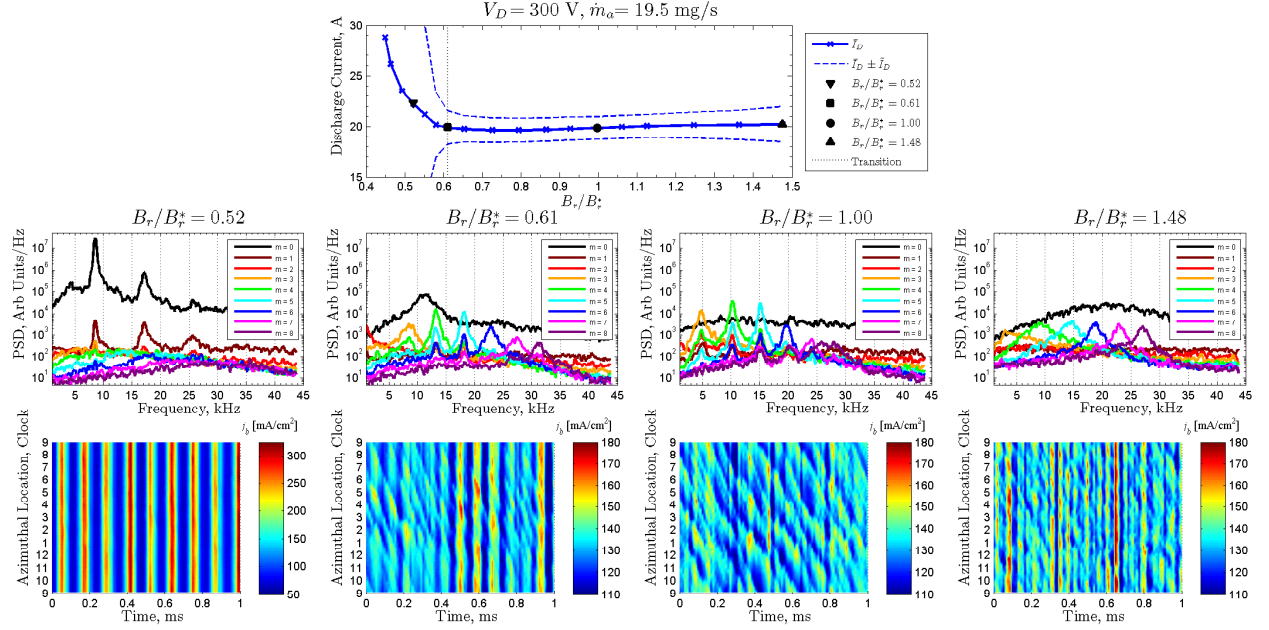


Figure 2: B-field sweep for 300 V, 19.5 mg/s showing transition at $B_r/B_r^* = 0.61$. The discharge current mean and oscillation amplitude are shown with the transition and for B_r/B_r^* settings selected for further analysis. The middle row plots are HIA PSDs and the bottom row plots are discharge current density. The scale range for $B_r/B_r^* = 0.52$ discharge current density is larger due to the magnitude of oscillations. A 500-Hz moving average filter has been applied to smooth all PSDs. Reproduced from Figure 17 of Ref. 7.

The modes are described in Ref. 7 as global oscillation mode and local oscillation mode. In global mode the entire discharge channel is oscillating in unison and spokes are either absent or negligible with discharge current oscillation amplitude (RMS) greater than 10% of the mean value. Downstream azimuthally spaced probes show no signal delay between each other and are very well correlated to the discharge current signal. In local oscillation mode perturbations in the discharge current density are seen to propagate in the $E \times B$ direction with clear spokes shown in a HIA PSD. The discharge current oscillation amplitude and mean values are significantly lower than global mode. Downstream azimuthally spaced probes show a clear signal delay between each other indicating the passage of spokes but are not well correlated to the discharge current indicating localized plasma oscillations within the discharge channel. The mode transitions were consistent across different tests and showed no hysteresis, but did change at different operating conditions. The transition between global mode and local mode occurred at higher B_r/B_r^* for higher mass flow rate or higher discharge voltage. The investigation did not conclude a mechanism that caused mode transitions, but that work is ongoing. The thrust was constant within experimental error through the mode transition but the thrust-to-power ratio decreased by 25% for the 14.7 mg/s flow rate; the peak in thrust-to-power occurred near the transition point. The plume showed significant differences between modes with the global mode significantly brighter in the channel and the near-field plasma as well as exhibiting a plasma spike on thruster centerline. For the external cathode case the plasma spike disappeared in local oscillation mode.

It was concluded that the H6 and likely any similar thruster should be operated in local oscillation mode to minimize discharge current and maximize performance. Thruster performance maps should include variation in discharge current, discharge voltage, magnetic field and flow rate to identify transition regions throughout the life of a thruster. Mode transitions provide valuable insight to thruster operation and suggest improved methods for thruster performance characterization.

III. Spoke Velocity Measurements

The spoke velocity can be calculated from either the high-speed imaging or the azimuthally spaced probes using several different methods. Spokes are observed to propagate at a range of velocities, so there is a distribution associated with the speed akin to a distribution function. The methods below will identify one representative velocity for spoke propagation.

A. Manual Method

Spokes are unambiguously observed in the FastCam videos and are obvious even to the casual observer as bright regions rotating azimuthally around the discharge channel. Using the McDonald technique to create a spoke surface,^{7,14} the spokes appear as diagonal stripes in the spoke surface as shown in Figure 11 of Ref. 7. This technique divides the discharge channel into 180 two-degree bins of averaged light intensity and a video consisting of N_{fr} frames will yield a $180 \times N_{fr}$ spokes surface.

The most obvious technique to calculate spoke velocity is to fit lines to the diagonal stripes on the spoke surface; the slope of which represent spoke angular velocity $\dot{\theta}_{sp}$ in deg/s. In the FastCam videos and subsequent video enhancement (c.f. Figures 2 and 3 from Ref. 16), spokes are observed to fill the entire channel width. Therefore, spoke angular velocity is converted to a linear velocity using the mean channel radius, R_{chnl}

$$v_{sp} = (2\pi R_{chnl}/360)\dot{\theta}_{sp} \quad (1)$$

In order to determine an average spoke angular velocity, 45 to 50 lines are manually fitted to a normalized spoke surface as shown in Fig. 3 for $B_r/B_r^* = 1.00$, 300 V and 19.5 mg/s. A normalized spoke surface shows the spokes more clearly without altering their characteristic slope. To normalize a spoke surface, each frame (vertical line) has its mean value subtracted and is divided by its RMS value. In order to test the uncertainty due to human error and repeatability, 50 lines were fitted to the same propagating spoke with a standard deviation of 39 m/s; this will be shown to be within the standard deviation of a typical velocity distribution. The velocity distribution for the spoke surface example of Fig. 3 is shown in Fig. 4 where the spoke velocity is 1530 ± 180 m/s and the uncertainty is the standard deviation of the distribution.

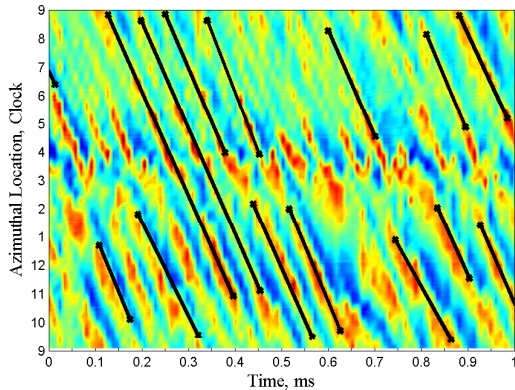


Figure 3: One millisecond segment of a normalized spoke surface showing 14 of 47 manually fitted lines for $B_r/B_r^* = 1.00$

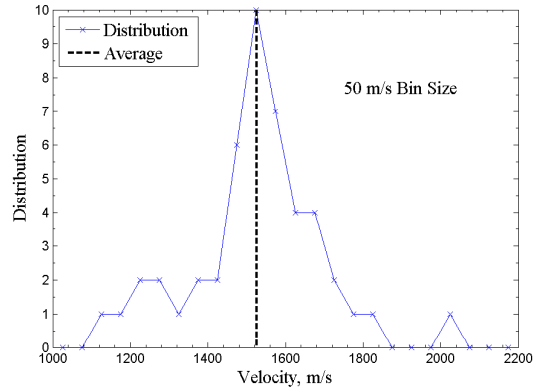


Figure 4: Velocity distribution for the manually fitted lines in Fig. 3. The black dashed line is the mean of the 47 measurements.

More sophisticated techniques will be introduced in later sections, but those results should be within the range of this straightforward, yet labor-intensive approach. Representative uncertainties for the manual method are the mean uncertainties in Fig. 9 of 190 m/s and 180 m/s for 300 V and 400 V, respectively.

B. Correlation Method

The correlation method uses linear cross-correlation to determine the time delay between oscillations in light intensity at different azimuthal locations in the discharge channel. The time delay represents transit time for a spoke to travel from one azimuthal location to another and is used to calculate angular and linear

velocity. By comparing a large quantity of azimuthal locations ($\mathcal{O}10^3$) a representative spoke velocity can be calculated.

Starting with the normalized spoke surface as discussed above, the time-history signal of light intensity for each bin is a $1 \times N_{fr}$ vector representing light fluctuations at that azimuthal location for the duration of the video which is typically 150 to 250 ms ($N_{fr} \sim 13 \times 10^3$ to 22×10^3). A 1 ms segment of four normalized light intensity traces are shown in Fig. 5 for reference. A linear cross-correlation analysis of the signals between two bins, b_j and b_k , at different azimuthal locations with an angular difference of $\Delta\theta_{j,k}$ degrees will yield the time, $t_{j,k}$, it took on average for a spoke to propagate around the channel from b_j to b_k . The cross-correlation function is¹⁷

$$R_{jk} = \lim_{T \rightarrow \infty} \frac{1}{T} \int_0^T b_j(t) b_k(t + \tau) dt \quad (2)$$

Signal delays for non-frequency dispersive propagation can be identified by peaks in R_{jk} where the highest peak is the time offset, $t_{j,k}$. Fig. 5 shows an example of the time offset for three azimuthal locations (30° , 50° and 70°) referenced to 12 o'clock on the thruster face calculated from linear cross-correlation. Five peaks in light intensity (spokes) are selected and shown how they propagate around the thruster in Fig. 5. The spoke velocity, $v_{spj,k}$, from b_j to b_k is

$$v_{spj,k} = (2\pi R_{chnl}/360)\Delta\theta_{j,k}/t_{j,k} \quad (3)$$

The spoke velocity for the correlation method is the mean spoke velocity calculated between N_{bins} compared

$$v_{sp} = \frac{1}{N_{bins}} \sum_j \sum_k v_{spj,k} \quad (4)$$

In principle, the spoke velocity can be calculated from the average time delay using every combination of the 180 bins, which would be over 32,000. However, practical considerations limit the range of bins that can be compared. The camera frame rate is 87,500 fps so each frame represents $11.4 \mu s$. A spoke traveling at 2000 m/s will travel 16° or 8 bins in the time span of one frame. Therefore, a practical lower limit is $\Delta\theta_{j,k} \geq 20^\circ$ or 10 bins. A single spoke typically propagates one-quarter of the discharge channel circumference for most B-field settings. In strong spoke regimes, a single spoke will propagate one-half to even the entire channel circumference. A reliable upper limit for automated processing is to only compare bins where $\Delta\theta_{j,k} \leq 70^\circ$ or 35 bins. In Fig. 5, 6 cycles can be identified in ~ 0.55 ms, which corresponds to ~ 11 kHz or a spoke period of $\tau_{sp} \sim 90 \mu s$. Due to signal noise, the cross-correlation peak occasionally matches to a spoke ahead or behind the correct spoke so the calculated offset time is in error by one or two τ_{sp} . Although this occurs more often when $\Delta\theta_{j,k} > 90^\circ$, it occasionally occurs for $\Delta\theta_{j,k} < 70^\circ$. These points are easy to identify via manual inspection, but reject criteria is set for automated data processing so any spoke velocity outside of 500 to 3500 m/s is rejected. In order to reduce computational time, only 90 bins (every other bin) are used for reference start points. All bins from bin 10 to 35 CCW from the reference bin are used for comparison. Therefore, j is 1, 3, 5, ... to 180 and k is 10 to 35 in Eq. (4) which yields a maximum of $N_{bins} = 2430$ possible points. The spoke velocities for smaller $\Delta\theta_{j,k}$ will have larger uncertainty because half of the camera frame period ($5.7 \mu s$) represents a large fraction of the spoke travel time ($\sim 14 \mu s$ to travel 20°). The standard deviation can be reduced by choosing a larger value for the lower limit of $\Delta\theta_{j,k}$ instead of 20° , but the number of points used in the calculation, N_{bins} , will also be reduced, so a balance must be reached.

Using the correlation method on the spoke surface in Fig. 3 yields a spoke velocity of $v_{sp} = 1470 \pm 270$ m/s where the uncertainty is the standard deviation of the velocities used in Eq. (4). This is within 4% of the

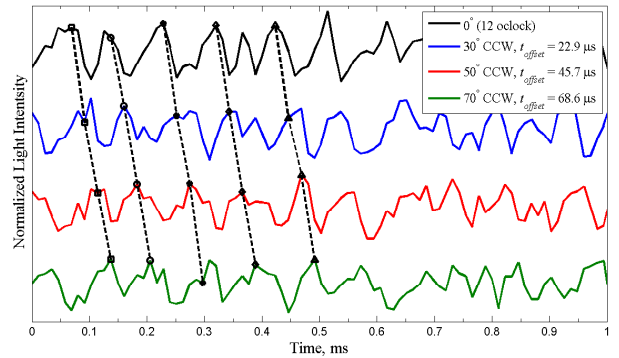


Figure 5: Light intensity traces for 4 azimuthal locations from the normalized spoke surface in Fig. 3. Selected locations are thruster 12 o'clock as the reference and 30° , 50° and 70° CCW from 12 o'clock. The offset times are calculated via linear cross-correlation from 12 o'clock to the other locations. Five peaks have been selected to demonstrate how spokes propagate CCW around the thruster using the calculated offset times.

manual technique described above. For this data point $N_{bins} = 2266$ of the possible 2430 points are used for $20^\circ \leq \Delta\theta_{j,k} \leq 70^\circ$. The manual method and correlation method produce very similar results as shown later in Figs. 7 and 9. Representative uncertainties for the correlation method are the mean uncertainties in Fig. 9 of 280 m/s and 260 m/s for 300 V and 400 V, respectively. The correlation method is important since it is an automated and reliable procedure of providing the same results as the laborious manual method.

C. Dispersion Relation Method

Dispersion relations are common place in plasma physics to describe the relationship between oscillation frequency and wave number. This method determines the spoke velocity from the phase velocity of an empirically determined dispersion relation. The 2-D Power Spectral Density (PSD) identifies a peak frequency for each spoke order, which is equivalent to wave number, and thus yields a dispersion plot from high-speed imaging results. An assumed functional form is fit to the data in order to calculate the numerical values for the dispersion relation.

The high-speed image analysis (HIA) method developed by McDonald¹⁸ and described in detail in Ref. 7 generates Power Spectral Densities (PSD) from the 2-dimensional spoke surface. Fig. 6. shows examples for the 300 V, 19.5 mg/s test case where peaks are clearly visible for each spoke order, m . As described by McDonald in his original derivation,¹⁴ m is analogous to number of wave lengths per channel circumference. Hence $m = 0$ or m_0 is no wave in the channel (the entire channel is dark or bright), $m = 1$ means one wave in the channel (one half bright, the other dark), $m = 2$ is two waves per channel (two bright regions, two dark regions), $m = 3$ is three waves per channel (three bright regions, three dark regions), etc. In the literature m is often called the wave mode, but we call it spoke order to avoid nomenclature confusion with the HET operational modes discussed in Section II. The azimuthal wave number, k_θ , is calculated from the spoke order by $k_\theta = m/r$. Fig. 6 shows each spoke order has a unique peak frequency that is typically 3-5 kHz higher than the previous m . Therefore, the HIA PSDs can be used to generate dispersion plots of peak frequency ω versus wave number k_θ .

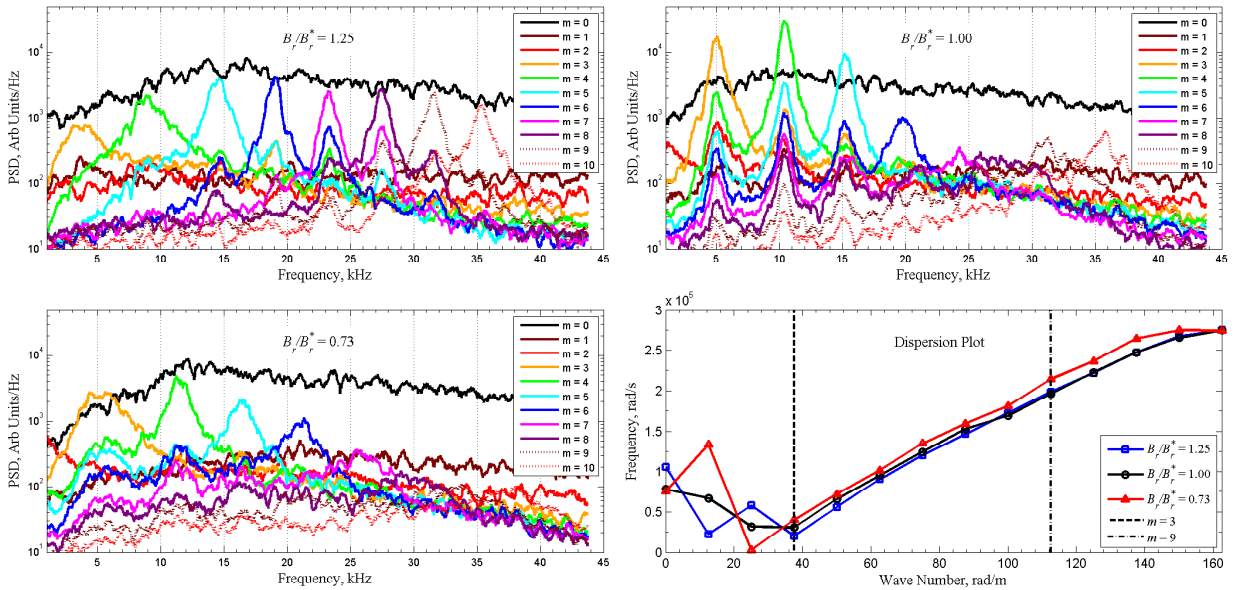


Figure 6: HIA PSDs for $B_r/B_r^* = 1.25$, 1.00 and 0.73 for 300 V and 19.5 mg/s with $m = 0 - 10$ shown. A 500 Hz moving average window has been applied to each PSD trace to reduce noise. Bottom right: the peak frequencies are identified and plotted versus wave number for corresponding dispersion relations.

The HIA PSDs are a powerful tool for understanding the plasma oscillations associated with HET operation. Ref. 19 showed that ion saturation reference probes identified the same peak frequencies as the HIA PSDs indicating that spoke related oscillations extended out into the plume. The same spoke surface that generated the normalized spoke surface in Fig. 3 was used to generate the HIA PSD for $B_r/B_r^* = 1.00$ in Fig. 6. Note the most dominant peak for $B_r/B_r^* = 1.00$ is $m = 4$ at 10.4 kHz, which is close the crudely

estimated frequency from Fig. 5 of ~ 11 kHz.

In order to automatically identify the peak frequencies for each spoke order, the PSDs are first smoothed with a 250 Hz moving average filter and the maximum value identified. Due to noise from the DFT the maximum value is not always the frequency at the center of the peaks seen in Fig. 6 so a Lorentzian ^a of the form

$$PSD(f) = \frac{A_0}{\pi} \frac{\frac{1}{2}\Gamma}{(f - f_0)^2 + (\frac{1}{2}\Gamma)^2} \quad (5)$$

is fitted to a segment of the PSD around the maximum value. The fit variables in Eq. 5 are the full-width at half maximum Γ , amplitude A_0 , and center frequency f_0 . This identifies the frequency f_0 or ω_0 at the center of the primary peak for each m . Example dispersion plots using this technique for the three HIA PSDs are also shown in Fig. 6.

For high magnetic field strength, $B_r/B_r^* = 1.25$, the higher spoke orders are most prominent with $m = 10$ showing a peak near the same height as $m = 5$. At the nominal setting, $B_r/B_r^* = 1.00$, the spoke orders $m = 3 - 5$ are an order of magnitude higher than $m \geq 6$, although peaks are visible up to $m = 10$. At the lowest magnetic field setting, $B_r/B_r^* = 0.73$, spoke orders $m = 3 - 5$ are still dominant but lower in magnitude than $B_r/B_r^* = 1.00$. Although very weak, peaks are still visible for $m = 6 - 9$. As magnetic field is increased, the frequency of each spoke order decreases as shown in the PSDs and dispersion plot in Fig. 6.

Dispersion relations can be of any functional form and can be quite complicated as will be discussed in the next section. However, we begin the analysis of HIA dispersion plots like the ones shown in Fig. 6, with a simple functional form

$$\omega^\alpha = c_1 k_\theta^\alpha + c_2 \quad (6)$$

where α is a power dependence and c_1 and c_2 are linear fit coefficients from a least-squares curve fit to the dispersion plots. Here only powers of $\alpha = 1$ and 2 will be considered, but higher powers are not precluded. In the spirit of the many elementary plasma waves found in homogenous plasmas, Eq. (6) can be written as a dispersion relation of the form

$$\omega^\alpha = v_{ch}^\alpha k_\theta^\alpha - \omega_{ch}^\alpha \quad (7)$$

where $v_{ch} = c_1^{1/\alpha}$ is a characteristic velocity such as ion acoustic speed or Alfvén speed and $\omega_{ch} = |c_2|^{1/\alpha}$ is a characteristic frequency such as the ion cyclotron frequency or plasma frequency. The unexpected minus sign in Eq. (7) results from the fact that c_2 is always less than zero for all fits. This can be seen from the example dispersion plots in Fig. 6 where the ordinate intercept is $\omega < 0$ when extrapolating backwards for $m < 2$ using the points from $3 \leq m \leq 12$. The physical implications of $c_2 < 0$ is a limit of $v_{ch}^\alpha k_\theta^\alpha > \omega_{ch}^\alpha$ for ω to be real, otherwise it will have a growing imaginary component and thus be unstable. This implies the only spoke orders that can exist are

$$m > R_{chnl} \frac{\omega_{ch}}{v_{ch}} = m_{min} \quad (8)$$

In practice, m_{min} is typically 3 or 4. The phase velocity, v_{ph} , and group velocity, v_{gr} , from the dispersion relation in Eq. (7) are

$$v_{ph} = \frac{\omega}{k_\theta} = \left[v_{ch}^\alpha - \left(\frac{\omega_{ch}}{k_\theta} \right)^\alpha \right]^{1/\alpha} \quad (9)$$

$$v_{gr} = \frac{\partial \omega}{\partial k_\theta} = v_{ph} \left(\frac{v_{ch}}{v_{ph}} \right)^\alpha \quad (10)$$

Eq. (9) shows that the phase velocity will always be less than the characteristic velocity and Eq. (10) shows the group velocity will always be greater than the phase velocity. In the limit of $(\omega_{ch}/(k_\theta v_{ch}))^\alpha \ll 1$ that follows from Eq. (8), a binomial expansion of Eq. (9) yields a simplified phase velocity

$$v_{ph} \simeq v_{ch} \left[1 - \frac{1}{\alpha} \left(\frac{\omega_{ch}}{k_\theta v_{ch}} \right)^\alpha \right] = v_{ch} \left[1 - \frac{1}{\alpha} \left(\frac{m_{min}}{m} \right)^\alpha \right] \quad (11)$$

With the FastCam frame rate at 87,500 fps the Nyquist limit is 43.8 kHz (2.75×10^5 rad/s) which is the asymptotic peak value for $m \geq 12$ observed in the dispersion plots of Fig. 6. In fitting the simple dispersion

^aRecommendation of M. McDonald for determining peaks in 2-D FFTs.

relation of Eq. 7 to the data in Fig. 6, a parametric study was done to determine the limits on m . Three different ranges were selected for spoke orders: $3 \leq m \leq 8, 9, 10$. In general the results were not sensitive to the upper limit of m used, but the $m = 8$ case had more variation in characteristic velocity. For all future comparison plots the range of m used for curve fitting will be $m = 3 - 9$ and $\alpha = 1, 2$ in Eq. (6).

The manual and correlation methods described above both identify a single, dominant spoke velocity for a given magnetic field setting and operating condition. However, the phase velocity from Eq. (9), which is assumed to be the spoke velocity, is a function of wave number. Fig. 7 shows v_{ph} as a function of spoke order m as a proxy for k_θ for 300 V and 400 V and $\alpha = 1, 2$ ($\alpha = 3$ is very similar to $\alpha = 2$ and is not shown). A single, representative spoke velocity can be calculated from a weighted average spoke velocity using the PSD value at the peak frequency f_m as the weighting factor w_m for each m . The spoke velocity and weighting factors are

$$v_{sp} = \sum_{m=5}^9 w_m v_{ph} \quad (12)$$

$$w_m = \frac{PSD(f_m)}{\sum_{m=5}^9 PSD(f_m)} \quad (13)$$

The HIA PSDs shown in Fig. 6 show that certain spoke orders are dominant at different magnetic field settings, with spoke orders $m = 4$ and 5 are dominant for $B_r/B_r^* < 1.0$. Fig. 7 shows for 300 V the phase velocities for $m = 3$ are far too low and for 400 V the the phase velocities for $m = 3$ and 4 are too low. The higher spoke orders are either dominant or the same magnitude as $m = 4, 5$ for the higher magnetic field settings. The weighting method of Eq. 13 accounts for the higher spoke order dominance at higher B_r/B_r^* values and causes the upward shift above ~ 1 , which tracks very well with the spoke velocities calculated via the manual and correlation method and builds confidence in the dispersion method. The minimum spoke order $m = 5$ was chosen in Eqs. (12) and (13) such that Eq. (8) is satisfied for all conditions. Fig. 7 shows the velocity from the correlation method typically follows the phase velocity for $m = 5$ or 6 closely for $B_r/B_r^*|_{trans} \leq B_r/B_r^* \lesssim 1.0$ and for $B_r/B_r^* \gtrsim 1.0$ the correlation velocity follows $m \geq 6$. Therefore using the phase velocities for $5 \leq m \leq 9$ to calculate a representative spoke velocity is reasonable. Using $4 \leq m \leq 12$ yields the same shape, but shifted lower by 100-200 m/s. Fig. 7 shows for 300 V both $\alpha = 1$ and 2 yield spoke velocities from the dispersion method that match the manual and correlation methods, but $\alpha = 2$ is better correlated for 400 V.

The standard error σ_{c_1} and σ_{c_2} for fit coefficients c_1 and c_2 in a linear, least-squared fit are easily calculated according to Ref. 20. Using the error propagation equation,²¹ the uncertainty in phase velocity from Eq. (9) for wave number k_θ is

$$\sigma_{v_{ph}} = \frac{v_{ph}}{\alpha} \left[\left(\frac{\sigma_{c_1}}{c_1} \right)^2 \left(\frac{v_{ch}}{v_{ph}} \right)^{2\alpha} + \left(\frac{\sigma_{c_2}}{c_2} \right)^2 \left(\frac{w_{ch}/k_\theta}{v_{ph}} \right)^{2\alpha} \right]^{1/2} \quad (14)$$

The total uncertainty in spoke velocity is calculated using the weighted average technique of Eqs. (12) and (13). For the same example used in Fig. 3 of $B_r/B_r^* = 1.00$, 300 V and 19.5 mg/s, the spoke velocity is 1510 ± 140 m/s for $\alpha = 1$ and 1570 ± 60 m/s for $\alpha = 2$. This is within 4% of the spoke velocity calculated with the manual method. Representative uncertainties for the dispersion relation method are the mean uncertainties in Fig. 9 of 120 and 47 m/s for $\alpha = 1$ and 2 at 300 V, and 157 and 41 m/s for $\alpha = 1$ and 2 at 400 V.

D. Probe Dispersion Relation

This section compares dispersion plots calculated from azimuthally spaced probes with dispersion plots described in the previous section. Azimuthally spaced probes can be used to determine the azimuthal wave number at a given frequency based on the phase delay between probe signals calculated from frequency domain transfer functions. The purpose of this calculation is to build confidence in the dispersion method by demonstrating a similarity in dispersion plots from two completely separate diagnostics measuring different locations: HIA observes the discharge channel and ISR probes observe the plume.

Lobbia initially showed that light intensity oscillations in the discharge channel were linearly related to electron density oscillations from 3 to 11 discharge channel radii downstream in a BHT-600.¹⁵ McDonald

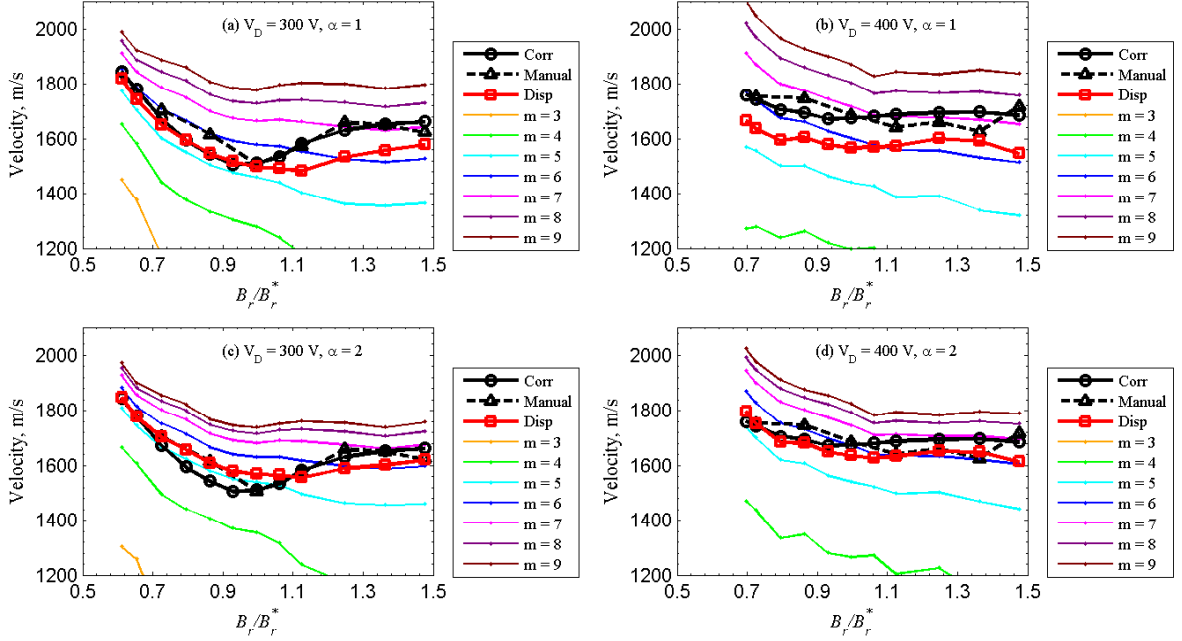


Figure 7: Comparison of phase velocities and spoke velocities for (a,c) 300 V and (b,d) 400 V, 19.5 mg/s for $\alpha = 1$ (a,b) and 2 (c,d). Colored lines represent the phase velocity for each spoke order m calculated with Eq. 9. Red lines with squares are spoke velocities calculated with the dispersion method and Eq. 12. Solid black lines with circles are spoke velocities calculated using the correlation method. Dashed black lines with triangles are spoke velocities calculated using the manual method.

conducted research on a segmented anode H6 where frequency oscillations in discharge current to the segmented anode correlated to oscillations observed with high-speed imaging.¹⁴ Recent research on the H6 demonstrated that downstream probes observe the same frequencies in plasma oscillations as the FastCam observes with light intensity oscillations in the channel.^{7,19} Therefore, plasma oscillations in the channel are related to oscillations observed downstream. In order to justify using a dispersion relation for the HIA results, a dispersion plot for downstream probes should be related to HIA dispersion plots.

Lobbia developed a frequency domain transfer function technique in order to calculate aggregate maps of electron density oscillations.²² The same technique is used to calculate a frequency domain transfer function between the ISR probes that yields gain and phase lag as a function of frequency. Note that we have employed set averaging as discussed by Lobbia,²³ which increases the signal-to-noise ratio and helps smooth out turbulent uncertainties. Unfortunately, this reduces the number of points for the Fourier transform by the number of sets averaged, which ultimately decreases the frequency resolution. For this analysis, the number of sets averaged is 75. The local azimuthal wave number at the probes is calculated from the phase lag, ϕ_{pr} , using the probe gap L_{pr} , by $k_\theta = \phi_{pr}/L_{pr}$.²⁴ Fig. 8 plots frequency versus azimuthal wave number for three conditions at 300 V (same conditions shown in Fig. 6) and one condition at 400 V for a 19.5 mg/s anode flow rate. Remarkably, the dispersion plots from probes 1.5 R_{chnl} downstream show striking similarities to the dispersion plots calculated from HIA analysis described in Section IIIC; the correlation appears strongest for $B_r/B_r^* = 1.25$ and 1.00. Note there appears to be an offset where the probe dispersion plots are a slightly higher frequency by $\sim 2 \times 10^4$ rad/s or ~ 3 kHz. This indicates that the same oscillations observed in the discharge channel with high-speed imaging are also detected in the plume as shown by PSD analysis in Ref. 19. This qualitatively builds confidence in the use of a dispersion relation to represent plasma oscillations from HIA.

E. Probe Delay Method

A final method to calculate spoke velocity is to calculate the time delay with linear cross-correlation of a signal passing from one azimuthally spaced probe to another. The downstream probes are azimuthally

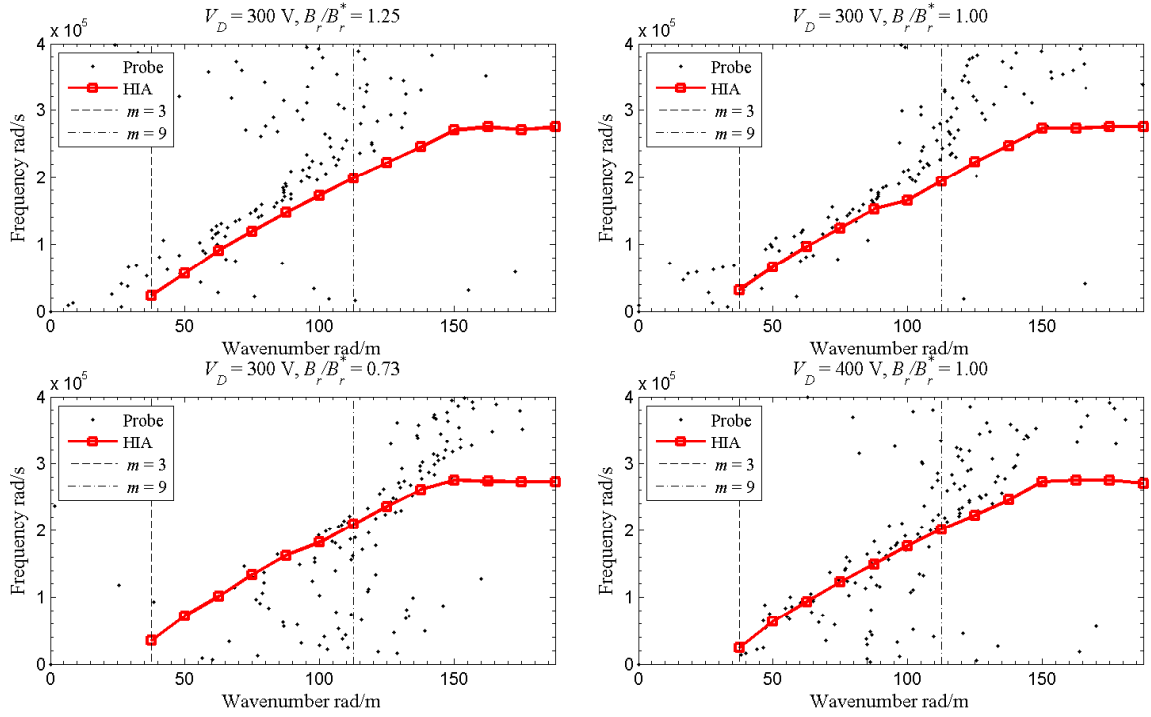


Figure 8: Probe dispersion plots for $B_r/B_r^* = 1.25$, 1.00 and 0.73 at 300 V, 19.5 mg/s and $B_r/B_r^* = 1.00$ for 400 V, 19.5 mg/s. The points are the dispersion plots from the phase lag between probes positioned $1.5 R_{chnl}$ downstream as a function of frequency and the red lines are the dispersion plots from HIA described in Section III C and shown in Fig. 6.

separated on channel centerline and observe the same plasma oscillations with a time delay. This time offset is converted to linear velocity based on the probe azimuthal spacing.

ISR probes are used to measure plasma oscillations in the plume that correlate to light intensity oscillations in the discharge channel. As discussed at length in Ref. 7, both ISR probes observed the same plasma oscillations, but in local mode the signal was delayed whereas in global mode the oscillations occurred nearly simultaneously at each probe. The time delay, t_d , was determined from a linear cross-correlation technique described in Section III B and Eq. 2. As shown in Figure 20c of that reference the time delay in local mode was between 10 and $15 \mu s$.

The spoke velocity can be calculated from the linear, azimuthal distance between each probe, $L_{pr} = (2\pi R_{chnl}/360)\Delta\theta_{1,2}$, divided by the time delay

$$v_{sp} = L_{pr}/t_d \quad (15)$$

The uncertainty in L_{pr} is calculated from the probe spacing uncertainty of 1.7° and the uncertainty of t_d is assumed to be 10% of the value.¹⁵ These uncertainties are used to calculate the maximum and minimum values for spoke velocity at a given setting $v_{sp}|_{min}^{max} = (L_{pr} \pm \sigma_{Lpr}) / (t_d \mp \sigma_{td})$. For the sample data point used in the previous methods of $B_r/B_r^* = 1.00$, 300 V and 19.5 mg/s the spoke velocity is 2090 ± 380 m/s, which is 38% higher than the spoke velocity calculated via the manual method. Representative uncertainties for the probe delay method are the mean uncertainties in Fig. 9 of 390 m/s and 420 m/s for 300 V and 400 V, respectively.

F. Spoke Velocity Comparison

Fig. 9 shows the spoke velocity calculated via all four methods discussed above with error bars for 300 V and 400 V at 19.5 mg/s flow rate. The manual, correlation and dispersion methods are all very well correlated. The spoke velocity from probe delay is consistently higher by $\sim 30\%$ for both conditions with the 400 V condition showing an unusual rise for $B_r/B_r^* > 0.9$. The reason for this divergence is unknown. The spoke

velocity is initially inversely dependent on B_r/B_r^* until $B_r/B_r^* \sim 1$ then levels out for higher magnetic field strength. The inverse dependence of v_{sp} on B_r/B_r^* is stronger for the 300 V condition than 400 V. Fig. 10 shows the characteristic velocities and m_{min} for the dispersion method for 300 V, 400 V and $\alpha = 1$ and 2. The characteristic velocities are higher for the $\alpha = 1$ and for $\alpha = 2$ they show the same inverse dependence on B_r/B_r^* until ~ 1 , after which they become level at the same value. The minimum spoke order appears to be linearly dependent on B_r/B_r^* with $\alpha = 2$ higher.

Fig. 11 shows a comparison of spoke velocities calculated from the correlation method for all five conditions tested. The 300 V, 19.5 mg/s condition is the average of four sweeps and the 400 V, 19.5 mg/s condition is the average of two sweeps. All conditions show the same trend of spoke velocity inversely dependent on B_r/B_r^* until $B_r/B_r^* \sim 1$. Power dependencies of $v_{sp} \propto (B_r/B_r^*)^{-0.5}$ and $v_{sp} \propto (B_r/B_r^*)^{-0.25}$ are shown in Fig. 11 for reference purposes only and were not generated from curve fits. The 300 V, 19.5 mg/s and 14.7 mg/s conditions show the strongest inverse dependence closer to the -0.5 reference, all others are closer to the -0.25 reference. For $B_r/B_r^* \gtrsim 1$, the 300 V, 14.7 mg/s condition still decreases, but not as steeply and 300 V, 19.5 mg/s actually increases velocity before stabilizing. All other conditions are essentially constant for the higher magnetic field settings. With the exception of 300 V, 14.7 mg/s, all conditions asymptote between 1600 and 1700 m/s for the maximum magnetic field settings. The trend of decreasing spoke velocity with increasing B_r/B_r^* for $B_r/B_r^* \lesssim 1$ is clear, but the velocity change is small, typically less than 25%. The variation in spoke velocity during a magnetic field sweep is on the order of the uncertainty, reinforcing that the dependence on magnetic field magnitude is not strong.

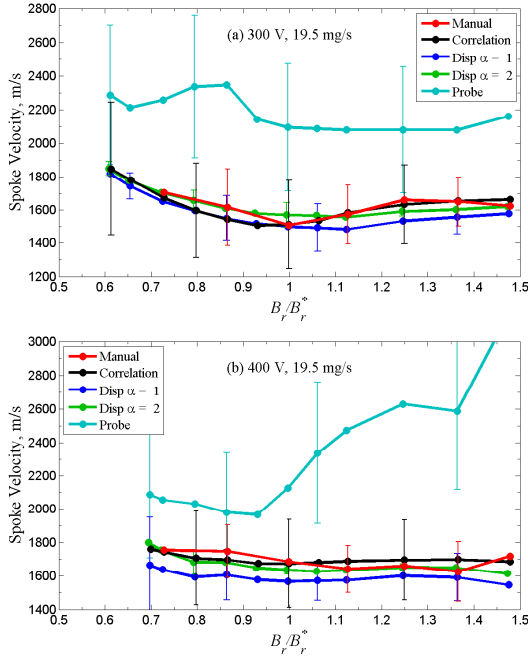


Figure 9: Comparison of spoke velocity calculation methods: manual, correlation, dispersion relation with $\alpha = 1, 2$ and probe delay method for (a) 300 V and (b) 400 V. Not all error bars are shown for clarity. For the dispersion relations, $m \geq 5$ has been used in Eqs. (12) and (13).

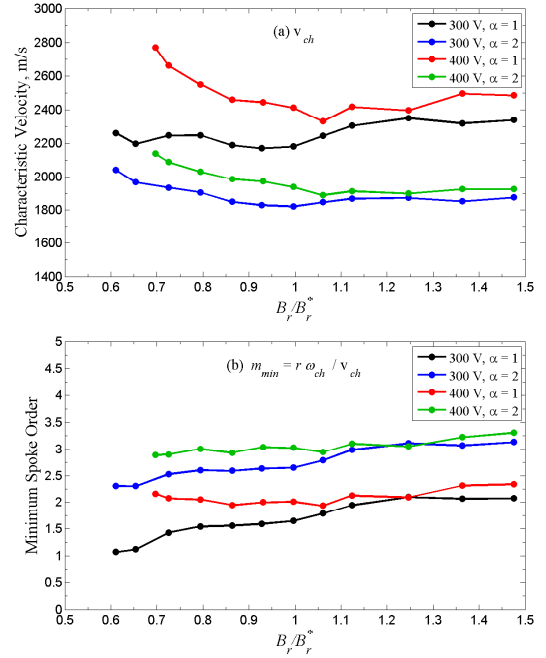


Figure 10: Comparison of the (a) characteristic velocity v_{ch} and (b) minimum spoke order from Eq. (8) for 300 V and 400 V, 19.5 mg/s. Power dependence $\alpha = 1$ and 2 are considered.

Combining the above discussion, we can state the following observations regarding spoke velocities; any theory on spoke mechanisms and propagation should account for these results.

1. Predict a spoke velocity that is 1500-2200 m/s in the H6; spoke velocity dependence on thruster size is unknown although likely weak as noted by McDonald.⁶ Spoke velocities are not dependent on discharge voltage or mass flow rate to within experimental error. Propagation is in the $E \times B$ direction.

- The dispersion relation can be approximated by a power law dependence $\omega^\alpha \sim v_{ch}^\alpha k_\theta^\alpha - \omega_{ch}^\alpha$ where $\alpha \geq 1$. The spoke velocity v_{sp} is less than the characteristic velocity v_{ch} and is dependent on the dominant spoke orders, typically $m > 4$. In general, the dominant spoke order increase with increasing magnetic field strength.
- Spoke velocity should be weakly, inversely dependent on magnetic field for $B_r/B_r^*|_{trans} < B_r/B_r^* \lesssim 1$. An example dependence of $v_{sp} \propto B^{-\beta}$ where $0.25 \lesssim \beta \lesssim 0.5$ is shown in Fig. 11, but other functional forms are possible. For $B_r/B_r^* \gtrsim 1$ the spoke velocity should nearly asymptote to a constant value.

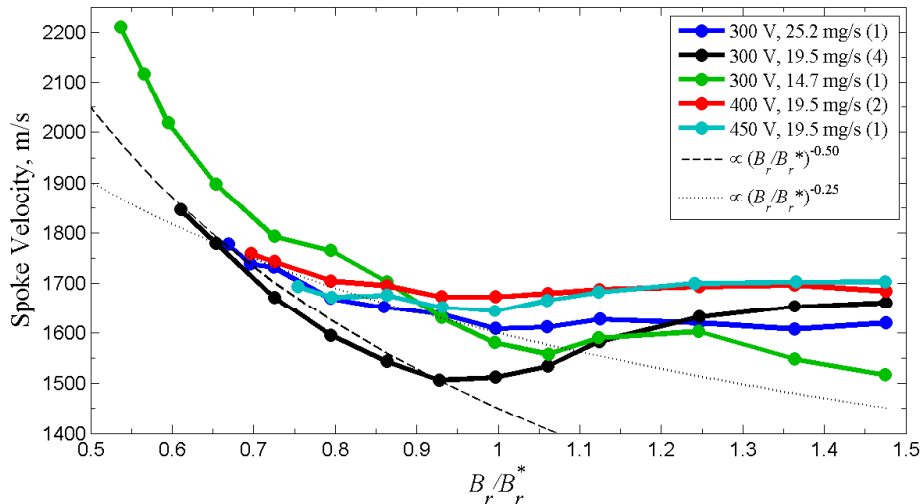


Figure 11: Spoke velocity calculated with the correlation method for all conditions tested. Parenthetical numbers are the number of B-field sweeps averaged together. Reference lines for possible functional forms of v_{sp} dependence on B_r/B_r^* are shown for discussion purposes only.

G. Spoke Velocity Observation Limits

Each spoke order represents the number of light and dark regions in the thruster so the wavelength is $\lambda = 2\pi R_{chnl}/m$. If the spoke travels 1/2 wavelength during the period of time the shutter is open, then the bright region will travel over the dark region rendering the spoke unobservable by the camera. Assuming the open period of the shutter is $\tau_s = 1/f_c$ where f_c is the camera frame rate, then the observable spoke velocity is

$$v_{sp} < \frac{\pi R_{chnl} f_c}{m} \quad (16)$$

For $m = 3, 5, 7$ and 9 , Eq. 16 yields maximum observable spoke velocities of 7300, 4400, 3100 and 2400 m/s, respectively. This is within all of the spoke velocities for each spoke order as shown in Fig. 7; however, the highest spoke orders are close to the limit.

IV. Mechanisms for Azimuthal Spokes

In this section we begin a discussion and investigation into the fundamental mechanisms of spoke formation and propagation. The mode transition investigation showed the presence of spokes is associated with improved thruster performance without determining causality,⁷ which motivates us to investigate the underlying fundamental physics. The previous section quantitatively identified some important characteristics of spoke propagation and developed a set of observations that any theory for spoke propagation must explain. Section IV.A broadly discusses and categorizes possible mechanisms for spoke formation as plasma waves that can be governed by a dispersion relation, a localized breathing mode oscillation, and wall effects. We first investigate plasma waves as a possible spoke formation mechanism. In Section IV.B and IV.C we identify time-averaged plasma measurements inside the H6 discharge channel at $B_r/B_r^* = 0.86$ from a

previous investigation²⁵ and the important characteristic frequencies. Section IV.D calculates and compares dispersion relations for homogeneous plasma waves and Section IV.E looks at drift waves and provides a detailed list of future dispersion relations to investigate. Section IV.F shows an interim summary of the dispersion relations considered thus far for plasma waves as the spoke formation mechanism.

A. Spoke Mechanisms and Locations

A coherent theory with supporting experimental evidence for spoke propagation has yet to emerge,²⁶ and the location in the plasma of their formation and mechanism for propagation are unknown. However, there have been no shortage of research published on azimuthal oscillations since the early work of Morozov, Tulinin and Espipchuk in the former Soviet Union and Janes and Lowder in the United States. Escobar recently provided an excellent overview of experimental, theoretical and numerical research on azimuthal oscillations,²⁷ and one should reference that work for a comprehensive discussion on spoke literature.

As mentioned previously, the location within the discharge channel where spokes originate is unknown. Previous experiments have detected azimuthal oscillations throughout the plasma from the anode out into the plume. The original work by Janes and Lowder¹ detected azimuthal oscillations with probes in the discharge channel where they even noted a spoke angle with respect to the walls. However, significant differences exist between their experimental apparatus in 1966 and the modern H6 including a longer discharge channel length, $\sim 1/2$ discharge voltage than nominal H6 values, chamber pressure two orders of magnitude higher, use of filament cathodes, radially inward magnetic field with over $2\times$ larger peak value, and quartz walls instead of Boron Nitride. More recent use of probes downstream of the discharge channel exit plane by Chesta²⁸ and Sekerak^{7,29} observed spokes propagating in the plume at least one channel diameter downstream. Work by McDonald¹⁴ with a segmented anode showed PSD frequency peaks for the discharge current from individual anode segments matched spokes frequencies from HIA PSDs. In a time history trace (Figure 9 from Ref. 14) local discharge current peaks are observed propagating from segment to segment at a velocity between 1700 and 2500 m/s. Therefore, the presence of azimuthal oscillations are detectable from the anode out into the plasma plume of HETs with theories and experiments disagreeing on where they originate.

In searching for the origin for spokes, we will consider the plasma in three different regions similar to that used in simulations:³⁰ near-anode region, the ionization/acceleration region near the channel exit, and near-field plasma plume. HETs have steep gradients in all relevant plasma parameters: density, electron temperature, electric field and magnetic field. However, the largest gradients occur near the channel exit where the magnetic field peaks and the bulk ionization and accelerations occurs. The origin and mechanism for spokes are unknown, but we will begin our discussion by broadly considering these different mechanisms:

1. **Plasma Waves** The values for the magnetic field, plasma density, neutral density, plasma potential and electron temperature vary in space throughout the discharge channel as will be shown later in Figs. 12 and 16 . However, if they are constant in time, slowly varying on time-scales longer than spoke propagation time-scales or have a small oscillation amplitude, then any number of plasma waves can propagate that can be described by a dispersion relation. Section V.C discusses the implications of this in more detail where the presence of spokes could be an indicator of breathing-mode damping. We can subdivide the plasma wave mechanisms into three categories:
 - (a) **(Nearly) Homogeneous Plasma Waves.** The gradients in the near-anode region or near-field plasma plume may be sufficiently small such that elementary, homogenous plasma waves may exist. Discussed in Section IV.D.
 - (b) **Drift Waves Driven by Gradients in the Plasma.** The ionization and acceleration region near the discharge channel exit has steep gradients in all plasma parameters and provides fertile ground for drift waves without considering ionization effects or neutral densities. A preliminary investigation for this is conducted in Section IV.E and a more comprehensive analysis of the plethora of drift dispersion relations (identified in Section IV.E.3) is reserved for future work.
 - (c) **Azimuthal Ionization Instability.** The spokes are bright regions moving azimuthally in the discharge channel as seen in high-speed imaging analysis, which would indicate spokes are regions of increased collisionality leading to more excited states that decay to release photons. From downstream ISR probes in the plume the spokes are observed as increased regions of plasma density. Together this may indicate that spokes are related to ionization processes. Chesta's³¹ and Escobar's²⁷ linear analyses showed oscillations due to ionization and Ref. 19 suggests that spokes

represent increased ion production zones. These waves are dependent on ionization frequencies and neutral density, which are captured in some of the dispersion relations identified in Section IV.E.3. Discussion of these mechanisms are reserved for future work.

2. **Localized Breathing Mode** Breathing mode oscillations are not small amplitude perturbations on a relatively steady value unlike the plasma waves in Item 1 that are derived from linearization. As discussed in Section V.C, simulations show that densities can vary by factors of order unity up to an order of magnitude. Detailed, time-resolved, internal plasma measurements of an HET discharge channel do not exist to verify the simulations. We can postulate that the same fundamental mechanism may exist between the spokes and breathing mode, where the breathing mode (global mode in Ref. 7) exhibits a uniform channel discharge and replenishment process while the spoke mode (local mode in Ref. 7) exhibits an azimuthally local discharge and replenishment process. As shown by several numerical simulations³²⁻³⁴ and in Fig. 14, the breathing mode is a slow progression of the neutral front down the channel leading up to a rapid ionization event that Barral³⁵ calls avalanche ionization. During the neutral replenishment period within the discharge channel, slight perturbations or azimuthal non-uniformities in electron density, electron temperature and/or neutral density (all related to ionization rate), cause a local region in the discharge channel to reach the avalanche ionization point before adjacent regions, thus causing a localized increase in plasma density. The localized electron density enhancement travels azimuthally in the $E \times B$ direction initiating avalanche ionization in an adjacent region thus propagating the perturbation in a cascade like event. Extensive numerical and experimental characterization of the neutral flow and plasma within the discharge channel was performed on the H6²⁵ where a primary ionization region of $\sim 25\%$ of the discharge channel length and neutral flow velocity of 250 m/s can be reasonably inferred. These assumptions yield a neutral refill time of the ionization region of $\sim 40 \mu\text{s}$, corresponding to a 25-kHz oscillation, which is in line with the oscillation frequencies observed. Breathing mode is typically lower frequency than spokes, so in breathing mode the neutral front could be receding deeper into the channel since neutral velocity is constant. Detailed investigation of this mechanism is reserved for future work.
3. **Wall Effects.** Previous research suggests that plasma contact with the wall^{10,36} or potentially wall heating⁷ could be related to spoke propagation and mode transition. Discussed briefly and only qualitatively in Section V.D.

B. H6 Internal Data

Internal measurements were made by Reid²⁵ on the H6 at 300 V with 20 mg/s anode flow rate after less than 300 hours of total thruster operation. The magnet settings used were $I_{IM} = 3.00\text{A}$ and $I_{OM} = 2.68\text{A}$, which corresponds to $B_r/B_r^* = 0.86$. Table 1 shows the source of internal data used for calculations in the following sections. These figures have been reproduced in Fig. 16(a)-(e) of the Appendix for reference. Fig. 12 shows the centerline plasma properties normalized by the maximum values. The electric field and electron temperature are nearly constant until $z/L_{chnl} \sim 0.8$, while the plasma density begins a significant increase at $z/L_{chnl} \sim 0.5$ and the region of peaked electron temperature is $z/L_{chnl} = 0.8 - 1.0$. The region of peaked electric field is $z/L_{chnl} = 1.0 - 1.2$, which constitutes the approximate acceleration zone.

Variable	Source	Notes
n_i	Reid ²⁵ Figure 7-10, 20 mg/s	Blended solution from OML and thin sheath Langmuir probe measurements
T_e	Reid ²⁵ Figure 7-5, 20 mg/s	Langmuir Probe, compare with Figure 15 from Hofer ¹³
V_p	Reid ²⁵ Figure 7-18, 20 mg/s	Emissive probe corrected with T_e from Langmuir probe, compare with Figure 15 from Hofer, ¹³ referenced to cathode
E_z	Reid ²⁵ Figure 7-21, 20 mg/s	Computed from derivative of plasma potential
n_n	Reid ²⁵ Figure 8-9, 20 mg/s	Computed from 1-D heavy particle continuity analysis

Table 1: Reference and notes for plasma measurements of H6 discharge channel (internal). Data are shown in Fig. 16(a)-(e) in the Appendix.

C. Frequencies

The frequencies of interest for this investigation are 5-15 kHz for breathing mode and 5-35 kHz for spokes. For comparison, the cyclotron frequency is $\omega_{ci,e} = |q|B/m_{i,e}$ and the plasma frequency is $\omega_{pi,e} = \sqrt{nq^2/(\epsilon_0 m_{i,e})}$, where subscript i is for ions and e is for electrons. Variables include q for the elementary charge, B for the magnitude of the magnetic field, $m_{i,e}$ are the ion and electron mass, n for the plasma density where quasi-neutrality has been assumed such that $n_i \simeq n_e \simeq n$, and ϵ_0 is the permittivity of free space. The lower hybrid frequency³⁷ is $\omega_{lh} \simeq \sqrt{\omega_{ci}\omega_{ce}}$ for $\omega_{pi} \gg \omega_{ci}$. Table 2 shows these characteristic frequencies at three different locations in the discharge channel $z = 0.25, 1.00$ and $1.5 L_{chnl}$ based on the data in Fig. 16, but can be summarized as: $\omega_{ci} \lesssim \omega < \omega_{lh} < \omega_{pi} < \omega_{ce} < \omega_{pe}$.

Now consider the empirically identified, approximate dispersion relation of Eq. 7 in Section III.C. The characteristic velocity, v_{ch} is shown in Fig. 10 to be between 2200 and 2800 m/s for $\alpha = 1$ and between 1800 and 2200 for $\alpha = 2$. In addition, Fig. 11 shows the spoke velocity or phase velocity is between 1500 and 2200 m/s for all tested operating conditions. The characteristic frequency, ω_{ch} , is typically a few times larger than the peak ion cyclotron frequency, ω_{ci} , but is within the same order of magnitude. We can now attempt to identify any frequencies in the 10's of kHz range and characteristic velocities or phase velocities that are in the range of ~ 2000 m/s. The following analysis and discussion assumes +1 ions, but multiply charged ions are known to exist in HETs. $E \times B$ probe measurements in the plume of the H6 showed probe currents for Xe^{2+} of 20% and Xe^{3+} of 10%, respectively, normalized to the maximum Xe^{1+} current.¹³

Oscillation	Units	$0.25L_{chnl}$	$1.00L_{chnl}$	$1.50L_{chnl}$
Ion cyclotron	kHz	0.25	1.7	1.3
Lower hybrid	kHz	120	810	650
Ion plasma	MHz	9.4	27	20
Electron cyclotron	MHz	61	400	320
Electron plasma	GHz	4.6	13	9.6

Table 2: Representative frequencies on channel centerline for Region I, II and III at $0.25, 1.00$ and $1.50 L_{chnl}$, respectively. Ion cyclotron and ion plasma frequencies are for Xe^{1+} .

D. Homogeneous Plasma Waves

Here we consider some simple drifts and homogeneous plasma waves that propagate perpendicular to magnetic fields such as $E \times B$ drift, electrostatic ion cyclotron waves and magnetosonic waves. Other waves summarized by the Clemmow-Mullaly-Allis diagram³⁸ that can propagate perpendicular to magnetic fields such as ordinary waves (O wave), extra ordinary waves (X waves) and upper-hybrid resonance are of higher frequency than the 10's kHz spoke oscillations.

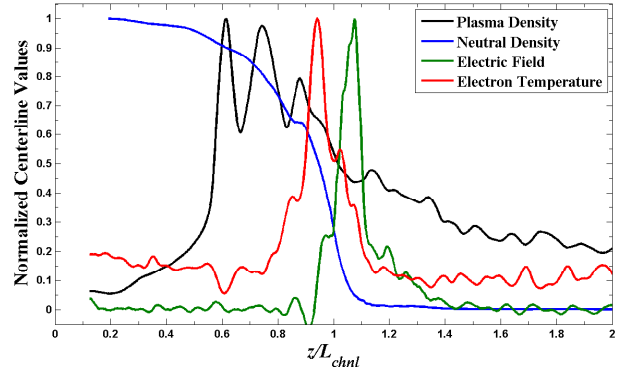


Figure 12: Centerline plasma properties based on the data in Fig. 16 from Reid.²⁵ All values have been normalized to the maximum value. A $0.025 L_{chnl}$ moving average window is applied to E_z and T_e , and $0.050 L_{chnl}$ window applied to n_i for smoothing. The multi-peaked structure of plasma density is likely experimental error and the values for neutral density are calculated.

1. $E \times B$ Drift

There are many single particle drifts to consider and only a few will be considered here; future work will investigate the ∇B and curvature drift. The $E \times B$ drift velocity and $\hat{\theta}$ and component are given by³⁹

$$\vec{v}_{E \times B} = \frac{\vec{E} \times \vec{B}}{|\vec{B}|^2} \quad (17)$$

$$v_{E \times B} \hat{\theta} = \frac{E_z B_r - E_r B_z}{B_r^2 + B_z^2} \quad (18)$$

The calculated $E \times B$ drift velocity distribution in the discharge channel is shown in Fig. 16(f) where the maximum value is over 4×10^6 m/s at the peak electric field and of order 10^5 m/s within $\pm 0.2 L_{chnl}$. These velocities are two to three orders of magnitude higher than the typical spoke velocity of 1500 to 2200 m/s. Fig. 13 shows the channel centerline values for $v_{E \times B}$ and v_{th_e} where the electron thermal velocity is the average of an assumed Maxwellian distribution³⁷ $v_{th_e} = \sqrt{8qT_e/(\pi m_e)}$ with T_e in eV. The region from $0.16 < z/L_{chnl} < 0.94$ is upstream from the ionization and acceleration zones with a mean value of 1.9×10^4 m/s and standard deviation of 8.4×10^4 m/s. Although the mean value is an order of magnitude larger than the spoke velocity, the large standard deviation (over 4 times the mean) is indicative of the experimental error and the $E \times B$ drift velocity could be of the same order as the spoke velocity in this region. However, the electric field would have to be small, $E_z \sim 0.01$ V/mm, for $v_{E \times B} \sim v_{sp}$ and is considered unlikely. Assuming the electrons follow a circular path on channel centerline, they would circle the thruster in $0.13 \mu s$ (8 MHz) at the peak $v_{E \times B}$ and $26 \mu s$ (38 kHz) upstream from the ionization region.

The electron thermal velocity is shown in Figs. 16(g) and 13, which is the same order of magnitude as the $E \times B$ drift velocity near the channel exit. The $E \times B$ drift velocity is greater than the thermal velocity for $1.0 < z/L_{chnl} < 1.1$ which is within the acceleration region. Outside of $0.9 < z/L_{chnl} < 1.4$, $v_{E \times B}/v_{th_e} < 0.1$ so the electron thermal velocity is an order of magnitude or larger than the $E \times B$ drift velocity throughout most of the channel and plume.

2. Electrostatic Ion Cyclotron Waves

Similar to sound waves in air, ion acoustic waves follow a simple dispersion relation

$$\omega = kv_s \quad (19)$$

where v_s is the ion acoustic speed with electrons of temperature T_e in eV

$$v_s = \sqrt{\frac{eT_e}{m_i}} \quad (20)$$

As shown in Fig. 16(c) the electron temperature in most of the channel and the near field plume is ~ 5 eV, except for near the exit plane $0.7 < L_{chnl} < 1.1$ where the electron temperature peaks at ~ 35 eV. The ion acoustic speed for $T_e = 5$ eV is 2000 m/s and for $T_e = 35$ eV is 5000 m/s. Fig. 16(h) shows the acoustic speed, which is close the characteristic speed of ~ 2000 m/s for most of the discharge channel. Unfortunately, ion acoustic waves propagate parallel to the magnetic field while spokes propagate perpendicularly.

An electrostatic ion cyclotron wave³⁸ is similar to an ion acoustic oscillation except the Lorentz force provides a restoring force³⁷ which yields a modification to Eq. 19

$$\omega^2 = k^2 v_s^2 + \omega_{ci}^2 \quad (21)$$

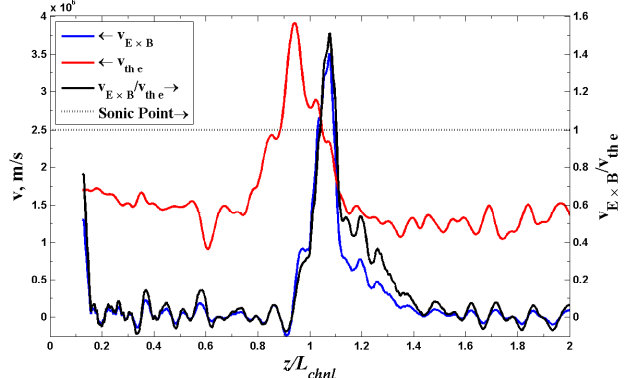


Figure 13: Left axis: Comparison of $E \times B$ drift velocity to electron thermal velocity on channel centerline from Figs. 16(f) and (g). A moving average window of $0.025 L_{chnl}$ has been applied to smooth the data. Right axis: The ratio is shown to indicate the $E \times B$ drift velocity is faster than the thermal velocity in the acceleration region ($z/L_{chnl} \sim 1.08$). The sonic point is $v_{E \times B} = v_{th_e}$.

Ion acoustic waves can propagate nearly perpendicular to B and have a phase velocity of

$$v_{ph} = \sqrt{v_s^2 + \omega_{ci}^2/k^2} \quad (22)$$

Except for the difference in sign inside the radical, note the similarity to Eq. 9 with $\alpha = 2$, the ion acoustic speed as the characteristic velocity and the ion cyclotron frequency as the characteristic frequency. Since the spoke location is unknown, spokes could be related to electrostatic ion cyclotron waves in the channel near the anode or in the near field plume region where $T_e \sim 5$ eV. A map of the electrostatic ion cyclotron frequencies is shown in Fig. 16(i) for k_θ corresponding to $m = 5$ where the frequencies are within the expected range for spokes. Unfortunately, this mechanism only implies that waves are perpendicular to the magnetic field (axial, CW azimuthal or CCW azimuthal) and does not force spokes to propagate in the $E \times B$ direction (CCW azimuthal for the H6).

3. Magnetosonic Waves

Magnetosonic waves are low frequency, electromagnetic waves propagating across the magnetic field. They are similar to acoustic waves, but the oscillations are produced by $E \times B$ drifts across E .³⁷ The phase velocity is

$$v_{ph} = c \sqrt{\frac{v_s^2 + v_A^2}{c^2 + v_A^2}} \quad (23)$$

where $v_A = B/\sqrt{\mu_0 m_i n}$ is the Alfvén speed and μ_0 is the permeability of free space. Fig. 16(j) shows the magnetosonic phase velocity (which is very close to the Alfvén speed so it is not shown in Fig. 16), both of which are an order of magnitude too large to be azimuthal spokes.

E. Gradient Drift Waves

Drift waves are common when spatial gradients exist in plasma properties because they provide free energy from which an instability can grow and a wave can propagate. Figs. 16 (a)-(e) clearly shows the plasma in the discharge channel and near-field plume are not uniform therefore spatial gradients exist, predominantly near the channel exit. There are many forms of drift waves that have been studied from fusion research. Here we start with the most common form of the drift wave that arises from a gradient in plasma density and proceed with increasing complexity. Also important is the definition of gradient length scale for parameter ρ

$$L_{\nabla \rho} = \left(\frac{1}{\rho} \frac{d\rho}{dz} \right)^{-1} \quad (24)$$

1. Density Gradient Drift Waves

The most fundamental gradient driven wave is the density gradient which assumes no steady state electric field and constant magnetic field, neither of which are fundamentally true in a HET discharge channel. The dispersion relation for density gradient drift waves and the diamagnetic drift velocity are³⁸

$$\omega = k_\theta v_{Drift} \quad (25)$$

$$v_{Drift} = \frac{T_e}{B} \frac{1}{n_e} \frac{dn_e}{dz} = \frac{T_e}{BL_{\nabla n_e}} \quad (26)$$

Drift waves are caused by density perturbations from ion $E \times B$ drift where ions “slosh” back and forth in the gradient (axial) direction, with the phase velocity in the $\nabla n_e \times B$ direction.³⁹ Therefore, no particles or energy are moving in the θ direction. In the H6, ∇n_e is in the $+z$ direction from the anode to $L < 0.8L_{chnl}$ and is in the $-z$ direction for $L > L_{chnl}$ from Fig. 16(a). Drift waves would be in the $E \times B$ for $L < 0.8L_{chnl}$ and in the $-E \times B$ for $L > L_{chnl}$. Spokes always propagate in the $E \times B$ direction, so we focus on the density gradient upstream from the ionization zone for density gradient waves to be the source of spoke motion.

The measured temperature in the discharge channel varies from 5 to 35 eV as shown in Fig. 16(c). Although the magnetic field magnitude and profile cannot be shown, it is of order 100’s of G similar to the SPT-100. Therefore, the T_e/B term in Eq. 26 is of order 10^3 , which is the same as the spoke velocity. The density length scale term $L_{\nabla n_e}$ must be of order unity for v_{Drift} to be in the spoke velocity range of

1500-2200 m/s. The experimental data from Reid in Fig. 16(a) for ion density on channel centerline shows an unexpected multi-peaked feature that is likely experimental error so the axial derivative of density is smoothed with a $0.06L_{chnl}$ moving average filter. The density gradient length scale is of order $L_{\nabla n_e} \sim 10^{-2}$ causing the drift velocity to be approximately two orders of magnitude too large. Discounting the unusual multi-peaked ion density yields a similar result where the density increases from 1×10^{18} to $4 \times 10^{18} \# / m^3 /$ in $0.2L_{chnl}$ which corresponds to $dn/dz = 3.6 \times 10^{20} \# / m^3 / m$ and $v_{Drift} \sim 10^5$ m/s. The drift velocity is shown in Fig. 16(k) for the entire discharge channel and is larger than the spoke or characteristic velocities we are seeking. It is interesting to note that this velocity is of the same order or lower than $E \times B$ drift velocity.

2. Collisional Density Gradient Drift Waves

The next step is to include collisional drift waves, which in the limit of small propagation along the B-field lines for a simple slab (cartesian coordinates) is³⁹

$$\omega = \frac{k_{\theta} v_{Drift}}{1 + k_{\theta}^2 v_s^2 / \omega_{ci}^2} \quad (27)$$

The phase velocity for Eq. 27 is shown in Fig. 16(l) for k_{θ} corresponding to $m = 5$, which yields results lower than the expected spoke velocity by as little as 50% to as much as an order of magnitude. Noting that $k_{\theta}^2 v_s^2 / \omega_{ci}^2 \gg 1$, Eq. 27 reduces to $\omega \sim \omega_{ci} / (k_{\theta} L_{\nabla n_e})$, which is not the same functional form as Eq. 7. Therefore, the spokes are unlikely caused by density gradient drift waves or collisional drift waves in a simplified slab geometry.

3. Future Investigation for Drift Waves

The body of literature on dispersion relations for various drift waves is voluminous and many other appropriate relations will be considered in the same manner as above. Future work will investigate the collisional drift instability in cylindrical coordinates as developed by Ellis,⁴⁰ which was successfully used by Jorns⁴¹ to identify drift waves related to cathode oscillations in magnetically shielded thrusters. Additionally, a drift relation shown by Esipchuk⁴² that accounts for density and magnetic field gradients has been used to reproduce azimuthal oscillations in the 10's kHz in the near-field plume of an SPT-100.²⁶ Kapulkin⁴³ developed a similar dispersion relation analysis for the near-anode region of an SPT-100, which is also very applicable to the H6 conditions tested here. Frias recently developed two new dispersion relations; one accounts for electron flow compressibility and the other includes temperature oscillations and gradients.^{44,45} The linearized 2-D axial-azimuthal models by Chesta³¹ and Escobar²⁷ that accounts for ionization and neutral density should be investigated. Finally, a dispersion relation developed by Ducrocq⁴⁶ to investigation high-frequency azimuthal oscillations has been used by Cavalier⁴⁷ to numerically investigate azimuthal waves and found modes that resemble ion acoustic waves. Applying all of these dispersion relations to the plasma parameters described above and comparing to the empirical dispersion analysis of Section III could yield valuable insight into the origin and nature of azimuthal spokes.

F. Interim Summary

An interim summary of the plasma drifts and waves discussed above is shown in Table 3. It must be emphasized that the discussion is not complete until the more complicated dispersion relations identified in Section IV.E.3 have been considered. However, it is helpful to identify which mechanisms have the potential to be responsible for azimuthal spokes.

V. Discussion

A. Spoke Velocities

The manual method, correlation method and dispersion method all yield very similar results for the spoke velocity building confidence in all three techniques. The manual and correlation methods do not require a selection of which spoke orders to consider, so they are more objective at determining a single, representative spoke velocity. The correlation method is preferred over the manual method due to ease of automation. In

Location	Upstream/Channel		Ion/Acceleration		Downstream/Plume	
Quantity	f	v	f	v	f	v
Units	Hz	m/s	Hz	m/s	Hz	m/s
Azimuthal spokes	2×10^4	2×10^3	2×10^4	2×10^3	2×10^4	2×10^3
Critical ionization velocity		4×10^3		4×10^3		4×10^3
$E \times B$ drift		2×10^4		4×10^6		3×10^4
Electron thermal velocity		2×10^6		4×10^6		2×10^6
Electrostatic ion cyclotron	2×10^4	2×10^3	4×10^4	5×10^3	1×10^4	2×10^3
Magnetosonic waves	8×10^4	1×10^4	2×10^5	2×10^4	2×10^5	2×10^4
Density gradient drift waves	8×10^5	1×10^5	-3×10^5	-4×10^4	-8×10^4	-1×10^4
Collisional drift waves	2×10^2	4×10^2	-6×10^2	-2×10^2	-7×10^2	-1×10^2

Table 3: Comparison of frequency and velocities for all drifts and waves considered in Section IV. The results are roughly divided into three axial regions: upstream of the primary ionization zone, ionization and acceleration region and the near-field plume downstream from the acceleration zone. Negative values indicate waves propagating in the $-E \times B$ direction or clockwise. For dispersion relation calculations, the k_θ used corresponds to $m = 4$.

the future, spoke velocities from the correlation method will be reported routinely as an additional metric with high-speed imaging data.

The inverse relation of spoke velocity to magnetic field is an interesting trend that should help identify the spoke mechanism even though the spoke velocity is only weakly dependent on magnetic field ($v_{sp} \propto B^{-\beta}$ where $0.25 \lesssim \beta \lesssim 0.5$). A previous study⁶ showed similar results, but the spoke velocity for each spoke order m was calculated from ω_m/k_θ (which effectively gives the characteristic velocity) instead of the more rigorous techniques used here. The results in Fig. 7(a) can be compared with Figure 5 from Ref. 6, which shows the same trend of decreasing spoke velocity up to point. However, the same H6 thruster was used and lower spoke orders were seen to dominate in that study for unexplained reasons. In contrast, the early work of Lomas⁴⁸ found that spoke velocity increased with magnetic field, which is contrary to what was observed by McDonald⁶ and in this investigation.

The $E \times B$ drift velocity also appears to have a simple $1/B$ dependence at first glance. However, noting that E is related to B from $E = \eta(1 + \Omega_e^2)j$ where η is the plasma resistivity, j is the discharge current density and Ω_e is the Hall parameter, means the dependence of $v_{E \times B}$ on B is actually more complicated. Spokes propagate in the $E \times B$ direction, so they may be related to electron or possibly even ion $E \times B$ drift. The Larmor radius for electrons is less than $0.05 L_{chnl}$ using their thermal velocity so they are magnetized as expected. The ion Larmor radius for +1 ions using the ion velocity calculated from plasma potential and energy conservation is greater than $10 L_{chnl}$ for most of the discharge channel except for the ionization region before they are accelerated by the large electric field. Note the Larmor radius for ions decreases for higher charge states, which are known to exist. If the ionization region is sufficiently offset upstream from the acceleration region, then a region of large ion density with relatively low ion velocity may exist ($< 5 \times 10^3$ m/s which is same order as spoke velocity). In this region, the ions may be able to undergo some azimuthal motion before being accelerated downstream, although unlikely completing a full cyclotron orbit. This motion could contribute to azimuthal spokes.

If the spokes are related to the $E \times B$ drift, then the results of Fig. 11 could provide insight into the electric field variations with magnetic field. For $B_r/B_r^* \lesssim 1$, the electric field may be approximately constant and the increase in magnetic field causes the spoke velocity to decrease. For $B_r/B_r^* \gtrsim 1$, the ratio of E/B may be approximately constant causing the spoke velocities to asymptote indicating the electric field is increasing with magnetic field.

The observation that ion acoustic speed matches the characteristic speed from the dispersion method is encouraging because v_s commonly appears in waves such as the electrostatic ion cyclotron wave and arises prominently in drift waves. In Escobar's simplified model that includes ionization,²⁷ the wave speed was found to be of order the ion acoustic speed and Cavalier recently found modes that resemble ion acoustic waves.⁴⁷ For $B_r/B_r^* = 0.86$, the spoke velocity is 1540 m/s from Fig. 11 and the characteristic velocities are

2190 and 1850 m/s for $\alpha = 1$ and 2 from Fig. 10(a). Fig. 14 shows a comparison of those velocities with the channel centerline ion acoustic velocity from Fig. 16(h) and the critical ionization velocity. Janes and Lowder suggested that the spokes may be related to the critical ionization velocity¹ first proposed by Alfvén and Ref. 6 contains a good discussion of the phenomenon and the implication to HETs. The critical ionization velocity for xenon is 4200 m/s and shown in Fig. 14, which is the same order of magnitude as the spoke velocity, but is still over twice the value. The ion acoustic speed matches the characteristic speed for $\alpha = 2$ better than $\alpha = 1$, particularly for $z/L_{chnl} < 0.7$. The spoke velocity is lower than the ion acoustic speed in the near-anode region, but is similar for the near field plume region. The similarity between ion acoustic speed and spoke velocity or characteristic velocity is unlikely a coincidence and will be further investigated with the more detailed dispersion relations discussed in Section IV.E.3.

B. High B-field Mode

The discussion in Section II identified two different modes for HET operation: global oscillation mode and local oscillation mode. However, the plasma oscillations in the discharge channel show different characteristics for high magnetic fields that may be indicative of yet another different operational mode. Previous simulations and experiments have observed changes in oscillations at high magnetic fields. In recent hybrid direct-kinetic simulations on an SPT-100, increasing the magnetic field oscillation above a threshold induced oscillations that Hara called the strong ionization mode.⁴⁹ In the first classification of modes, Tilinin⁹ also noted larger oscillations in discharge current at high magnetic field settings that he called macroscopic instability or magnetic saturation regimes. It should be noted the device used in Tilinin’s study pre-dated the SPT-100 and may have limited applicability.

Fig. 2 shows that as the magnetic field is increased, the spoke order increases, the spoke duration decreases and low-amplitude oscillations occur throughout the channel. Additionally, Figures 12 and 13 of Ref. 7 show the discharge current RMS increases at high magnetic field settings for all conditions except 300 V, 25.2 mg/s. Finally, Fig. 11 shows that spoke velocity becomes independent of magnetic field for $B_r/B_r^* \gtrsim 1$. The transition to this mode is not as sharp as the distinct transition between global and local mode. A qualitative explanation can be offered if collisional drift waves are responsible for azimuthal spokes. In discussing collisional drift waves, Bellan notes³⁹ “plasmas with strong magnetic fields tend to have turbulent, short perpendicular wavelength drift waves, whereas plasmas with weak magnetic fields have coherent, long perpendicular wavelength drift waves.” However, the differences in magnetic field strength we are considering are factors of 2 or less and not orders of magnitude different. Regardless, this could indicate that the high magnetic field settings are a turbulence dominated oscillation mode.

C. Breathing Mode Damping

The investigation on HET mode transitions⁷ showed that spokes were present and dominated plasma oscillations when the global oscillation ceased. We can postulate that the global oscillation mode is the well-studied breathing mode and the transition to local oscillation mode represents a damping or cessation of the breathing mode mechanism allowing the azimuthal spokes to propagate. This would mean that the transition from global mode to local mode is an indication that the ionization front has been stabilized axially in the discharge channel. The breathing mode has been numerically modeled by Fife,³² Boeuf,³³ Barral³⁴ and Hara.⁵⁰ However, Choueri²⁶ pointed out in 2001 that stability criteria has yet to be theoretically developed. Barral⁵¹ recently published the first known stability analysis for the breathing mode using linear and non-linear techniques, but further validation is necessary to confirm the criteria.

All of the preceding analysis on spoke propagation and dispersion relations assumes the plasma properties are constant in time within the discharge channel allowing spokes to propagate. In the H6, a typical spoke

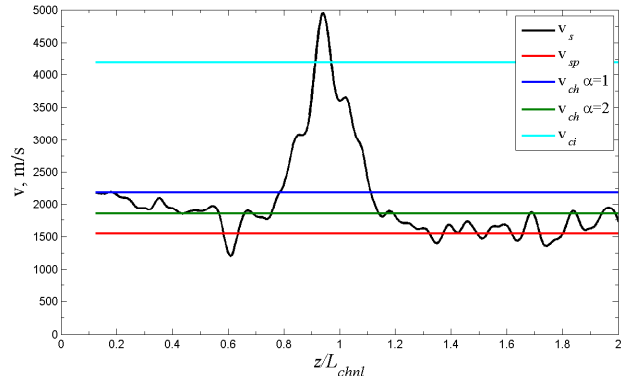


Figure 14: Ion acoustic speed on channel center line for $B_r/B_r^* = 0.86$ from Fig. 16(h) smoothed by a 0.038 z/L_{chnl} moving average filter. The critical ionization velocity, spoke velocity and characteristic velocities for $\alpha = 1, 2$ are shown for comparison.

will require $\sim 300 \mu\text{s}$ to travel around the entire discharge channel. The 1-D fluid simulation of an SPT-100 developed by Barral³⁴ shows that during a $\sim 100 \mu\text{s}$ breathing mode cycle the plasma properties can change significantly. Fig. 15 for the plasma properties on discharge channel centerline shows that neutral density can change by a factor of 2-3, plasma density can change up to an order of magnitude, and electron temperature can change by a factor of 2 (from Figure 5 of Ref. 34, not reproduced here). The simulation calculated a slow progression of the neutral front down the discharge channel building up to avalanche ionization. Fig. 15 shows that once avalanche ionization occurs at $\sim 50 \mu\text{s}$ and again at $\sim 150 \mu\text{s}$, the plasma density peaks and the neutral front recedes with a velocity in the range of $0.5 - 5 \times 10^3 \text{ m/s}$. Spokes may not be able to propagate since the breathing mode period is of the same order or smaller than the time required for spoke propagation and the recession rate can be greater than the spoke velocity of $\sim 1700 \text{ m/s}$.

A related paper at this conference by Hara⁴⁹ uses a hybrid direct-kinetic simulation to vary magnetic field and induce a mode transition in an SPT-100 type thruster. There it is found that the breathing mode is damped in a region of optimal performance similar to the experimental results of Ref. 7. A future publication will investigate the breathing mode frequency variation and transition criteria using a fluid model. The results from Ref. 7 will be combined with the 1-D transient fluid code in Ref. 34 to experimentally and computationally investigate breathing mode stability and assess whether HET mode transitions are indeed breathing mode damping.

D. Wall Considerations

A HET does not naturally have a radial restoring force like a magnetron so the electrons likely interact with the wall in some way (magnetic mirror or radial electric field) to propagate their motion to make HETs closed-drift devices. Recent research shows that plasma contact with the wall or potential wall heating could be related to spoke propagation and mode transition. The transition between modes was noted to be affected by time at the given operating condition, which could be related to wall heating and thermal equilibrium,⁷ although wall temperatures were not measured in that investigation. Additionally, while investigating magnetically shielded thrusters that have reduced plasma-wall interactions, Jorns⁴¹ did not observe spokes. The magnetically shielded H6 showed similar performance to the unshielded H6¹³ suggesting the spokes are only prominent in non-magnetically shielded thrusters. Additionally, thrusters with partial ceramic walls (boron nitride near the channel exit/ionization zone and conducting walls near the anode) may show different spoke behaviors if wall effects are important. Evidence of these different behaviors will be investigated in future work.

While investigating different wall materials in the SPT-100, Gascon¹⁰ observed mode transitions similar to those observed in Ref. 7. Gascon did not have the ability to observe spokes in that investigation so we cannot confirm that spokes were present in the low discharge current mode. The accompanying theory provided by Barral³⁶ suggested Space Charge Saturation, when the wall secondary electron emission coefficient approaches unity, was responsible for the mode transition. If this is correct, it implies a wall related phenomenon for mode transition and hence the onset or disappearance of spokes.

Even though we do not have a proven theory for spoke formation and propagation, we can speculate that the electron $E \times B$ drift motion inherent in HET discharge channels is related to spokes since spokes always propagate in the $E \times B$ direction. As was discussed by King⁵² based on single particle motion, a radial electric field at the outer wall is required to keep the electrons on a circular path in the discharge channel due to the cylindrical geometry. Katz^b pointed out that the sinusoidal motion suggested by King

^bPersonal correspondence.

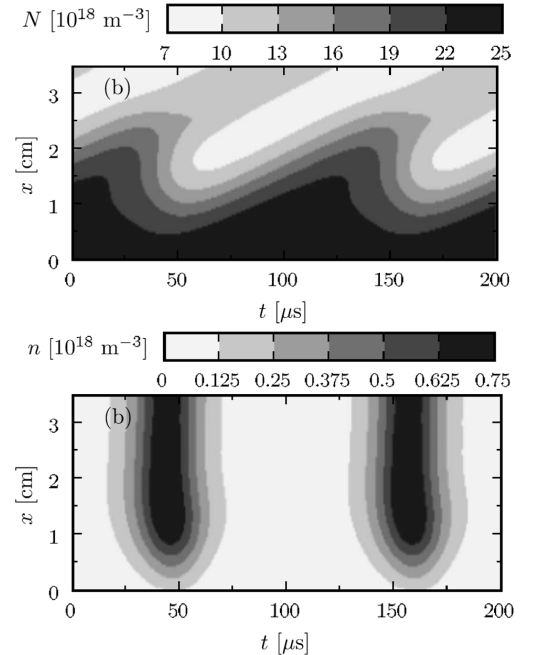


Figure 15: Neutral density (top) and plasma density (bottom) from 1-D fluid simulation of an SPT-100 on channel centerline. x direction is axial distance on channel centerline with the anode at $x = 0$. Reproduced from Figure 3(b) and 4(b) of Ref. 34.

is likely not accurate because the electrons would spend more time at the extrema (inner and outer walls) causing the electron density to peak off-channel centerline which is not seen in Fig. 16(a). We can calculate the electric field required to keep the electrons in a circular path following the discharge channel walls from simple centripetal acceleration. Considering the $E \times B$ drift velocity and the electron thermal velocity, the range of azimuthal electron velocities v_θ to consider is 1×10^4 to 5×10^6 m/s. Using the electron equation of motion, the radial electric field $E_r = (m_e/q)(v_\theta^2/R_{outer})$ required for the electron to maintain circular motion at the outer wall is $6 \mu\text{V}/\text{mm}$ to $1.5 \text{ V}/\text{mm}$. This is a small electric field that could be established by sheaths at the walls or internal to the plasma in order to maintain quasineutrality and the electrons are likely in nearly circular motion around the discharge channel. Regardless, a radial electric field at the walls is required to reflect electrons back into the channel per King or is required to keep electrons in a circular motion around the discharge channel. If this field cannot be established or becomes perturbed, then the electron motion around the discharge channel could be disrupted, which could disrupt spoke propagation assuming they are related.

VI. Conclusions

The spoke velocity is determined using three methods with similar results: manual fitting of diagonal lines on the spoke surface, linear cross-correlation between azimuthal locations and an approximated dispersion relation. The spoke velocity for three discharge voltages (300, 400 and 450 V) and three anode mass flow rates (14.7, 19.5 and 25.2 mg/s) yields spoke velocities between 1500 and 2200 m/s across a range of normalized magnetic field settings. The spoke velocity is inversely dependent on magnetic field strength for $B_r/B_r^* \lesssim 1$ and asymptotes to 1600-1700 m/s for $B_r/B_r^* \gtrsim 1$ for all conditions except 300 V, 14.7 mg/s. The dispersion plots for probes 1.5 R_{chnl} downstream displays similarities to the dispersion plots calculated from HIA reinforcing previous results that oscillations observed with imaging of the discharge channel are correlated to oscillations in the plasma plume. Spoke velocity from the probe delay method is $\sim 30\%$ higher for 300 V, 19.5 mg/s and for 400 V, 19.5 mg/s shows an unexplained increase for $B_r/B_r^* > 0.9$.

The mechanism for spoke formation is unknown although we consider plasma waves (homogeneous plasma, gradient driven drifts, or ionization related instabilities), a localized breathing mode, or wall-effects. It is unknown whether spokes originate in the near-anode, ionization/acceleration region or the near-field plume so the plasma properties from previous internal measurements at $B_r/B_r^* = 0.86$ are used to investigate various dispersion relations. The 10's of kHz oscillations associated with spokes are compared to standard plasma oscillations showing $\omega_{ci} \lesssim \omega < \omega_{lh} < \omega_{pi} < \omega_{ce} < \omega_{pe}$. The velocities and frequencies are compared to standard plasma waves such as $E \times B$ drift, electrostatic ion cyclotron, magnetosonic and various drift waves. The $E \times B$ drift is two to three orders of magnitude larger than the spoke velocity and is of the same magnitude as the electron thermal velocity in agreement with previous results. Electrostatic ion cyclotron waves are of the same frequency as spokes. The empirically approximated dispersion relation of $\omega^\alpha = v_{ch}^\alpha k_\theta^\alpha - \omega_{ch}^\alpha$ where $\alpha \geq 1$ yields a characteristic velocity that matches the ion acoustic speed for ~ 5 eV electrons that exist in the near-anode and near-field plume regions of the discharge channel. Simple, cartesian coordinate density gradient drift waves have a diamagnetic drift velocity that is ~ 2 orders of magnitude higher and simple slab collisional drift waves phase velocities are too low. While a good start, these simple dispersion relations do not cover the extensive body of literature on drift waves, particularly those that have been derived for HETs recently, and a more extensive comparison effort is underway that will be presented in future publications.

Acknowledgments

The author (M. Sekerak) acknowledges this work was supported by a NASA Office of the Chief Technologist's Space Technology Research Fellowship (NSTRF). This work was also supported by AFOSR and AFRL through the MACEEP center of excellence grant number FA9550-09-1-0695. Dr. Mitat Birkan of AFOSR (and author Dr. Daniel Brown) is the MACEEP program manager. Support was also provided by project F033162 from subcontract RS130040 awarded by ERC, Inc. A portion of this research was carried out at the Jet Propulsion Laboratory, California Institute of Technology, under a contract with the National Aeronautics and Space Administration. The authors would like to thank three former PEPL students: Dr. Robert Lobbia for development of the HDLP, Dr. Michael McDonald for development of the FastCam Analysis and Dr. Bryan Reid for his internal measurements. Finally, Marcel Georgin's tedious manual spoke

velocity calculations are appreciated.

References

- ¹Janes, G. S. and Lowder, R. S., "Anomalous Electron Diffusion and Ion Acceleration in a Low-Density Plasma," *Physics of Fluids*, Vol. 9, No. 6, 1966, pp. 1115.
- ²Raitses, Y., Griswold, M., Ellison, L., Parker, J., and Fisch, N., "Studies of Rotating Spoke Oscillations in Cylindrical Hall Thrusters," AIAA 2012-4179, *48th AIAA/ASME/SAE/ASEE Joint Propulsion Conference*, Atlanta, GA, Aug. 2012.
- ³Ellison, C. L., Raitses, Y., and Fisch, N. J., "Cross-field electron transport induced by a rotating spoke in a cylindrical Hall thruster," *Physics of Plasmas*, Vol. 19, No. 1, 2012.
- ⁴Parker, J. B., Raitses, Y., and Fisch, N. J., "Transition in electron transport in a cylindrical Hall thruster," *Applied Physics Letters*, Vol. 97, No. 9, 2010, pp. 091501.
- ⁵Brown, D. and Gallimore, A., "Investigation of Low Discharge Current Voltage Hall Thruster Operating Modes and Ionization Processes," IEPC-2009-074, *31st International Electric Propulsion Conference*, Ann Arbor, MI, Sept. 2009.
- ⁶McDonald, M. and Gallimore, A., "Parametric Investigation of the Rotating Spoke Instability in Hall Thrusters," IEPC-2011-242, *32nd International Electric Propulsion Conference*, Wiesbaden, Germany, Sept. 2011.
- ⁷Sekerak, M. J., Hofer, R. R., Polk, J. E., Longmier, B. W., Gallimore, A., and Brown, D. L., "Mode Transitions in Hall Effect Thrusters," AIAA 2013-4116, *49th AIAA/ASME/SAE/ASEE Joint Propulsion Conference*, American Institute of Aeronautics and Astronautics, July 2013.
- ⁸Morozov, A. I., "The conceptual development of stationary plasma thrusters," *Plasma Physics Reports*, Vol. 29, No. 3, March 2003, pp. 235-250.
- ⁹Tilinin, G. N., "High-frequency plasma waves in a Hall accelerator with an extended acceleration zone," *Soviet Physics-Technical Physics*, Aug. 1977.
- ¹⁰Gascon, N., Dudeck, M., and Barral, S., "Wall material effects in stationary plasma thrusters. I. Parametric studies of an SPT-100," *Physics of Plasmas*, Vol. 10, No. 10, 2003, pp. 4123.
- ¹¹Reid, B. M., Shastry, R., Gallimore, A. D., and Hofer, R. R., "Angularly-Resolved EB Probe Spectra in the Plume of a 6-kW Hall Thruster," AIAA 2008-5287, *44th AIAA/ASME/SAE/ASEE Joint Propulsion Conference & Exhibit*, Hartford, CT, July 2008.
- ¹²Walker, M. L. R., *Effects of Facility Backpressure on the Performance and Plume of a Hall Thruster*, Ph.D. dissertation, University of Michigan, Ann Arbor, MI, 2005.
- ¹³Hofer, R., Goebel, D., Mikellides, I., and Katz, I., "Design of a Laboratory Hall Thruster with Magnetically Shielded Channel Walls, Phase II: Experiments," AIAA 2012-3789, *48th AIAA/ASME/SAE/ASEE Joint Propulsion Conference & Exhibit*, Atlanta, GA, Aug. 2012.
- ¹⁴McDonald, M., Bellant, C., St Pierre, B., and Gallimore, A., "Measurement of Cross-Field Electron Current in a Hall Thruster Due to Rotating Spoke Instabilities," AIAA 2011-5810, *47th AIAA/ASME/SAE/ASEE Joint Propulsion Conference & Exhibit*, San Diego, CA, Aug. 2011.
- ¹⁵Lobbia, R., Liu, T., and Gallimore, A., "Correlating time-resolved optical and Langmuir probe measurements of Hall thruster dynamics," SPS-III-36, *JANNAF 3rd Spacecraft Propulsion Joint Subcommittee Meeting*, Orlando, FL, Dec. 2008.
- ¹⁶McDonald, M. S. and Gallimore, A. D., "Rotating Spoke Instabilities in Hall Thrusters," *IEEE Transactions on Plasma Science*, Vol. 39, No. 11, Nov. 2011, pp. 2952-2953.
- ¹⁷Bendat, J. S. and Piersol, A. G., *Engineering applications of correlation and spectral analysis*, Wiley, New York, 1980.
- ¹⁸McDonald, M., *Electron Transport in Hall Thrusters*, Ph.D. dissertation, University of Michigan, Ann Arbor, MI, 2012, Applied Physics-note.
- ¹⁹Sekerak, M. J., McDonald, M. S., Hofer, R. R., and Gallimore, A. D., "Hall Thruster Plume Measurements from High-Speed Dual Langmuir Probes with Ion Saturation Reference," IEEE-2013-2129, *34th IEEE Aerospace Conference*, Big Sky, MT, March 2013.
- ²⁰Acton, F. S., *Analysis of straight-line data.*, Wiley, New York, 1959.
- ²¹Bevington, P. R. and Robinson, D. K., *Data reduction and error analysis for the physical sciences*, McGraw-Hill, New York, 1992.
- ²²Lobbia, R. B., *A Time-resolved Investigation of the Hall Thruster Breathing Mode*, Ph.D. dissertation, University of Michigan, Ann Arbor, MI, Jan. 2010.
- ²³Lobbia, R. B. and Gallimore, A. D., "Fusing Spatially and Temporally Separated Single-point Turbulent Plasma Flow Measurements into Two-dimensional Time-resolved Visualizations," *12th International Conference on Information Fusion*, Seattle, WA, July 2009.
- ²⁴Beall, J. M., "Estimation of wavenumber and frequency spectra using fixed probe pairs," *Journal of Applied Physics*, Vol. 53, No. 6, 1982, pp. 3933.
- ²⁵Reid, B. M., *The Influence of Neutral Flow Rate in the Operation of Hall Thrusters*, Ph.D. dissertation, University of Michigan, Ann Arbor, MI, 2009.
- ²⁶Choueiri, E. Y., "Plasma oscillations in Hall thrusters," *Physics of Plasmas*, Vol. 8, No. 4, 2001, pp. 1411.
- ²⁷Escobar, D. and Ahedo, E., "Ionization-induced azimuthal oscillation in Hall Effect Thrusters," IEPC-2011-196, *32nd International Electric Propulsion Conference*, Wiesbaden, Germany, Sept. 2011.
- ²⁸Chesta, E., Lam, C., Meezan, N., Schmidt, D., and Cappelli, M., "A characterization of plasma fluctuations within a Hall discharge," *IEEE Transactions on Plasma Science*, Vol. 29, No. 4, Aug. 2001, pp. 582-591.
- ²⁹Sekerak, M. J., Gallimore, A. D., and Polk, J. E., "High-speed Dual Langmuir Probe with Ion Saturation Reference (HDLP-ISR) for Hall Thruster Plume Measurements," *NASA Technology Days*, Cleveland, OH, Nov. 2012, Poster.

- ³⁰Hofer, R., Katz, I., Mikellides, I., Goebel, D., Jameson, K., Sullivan, R., and Johnson, L., “Efficacy of Electron Mobility Models in Hybrid-PIC Hall Thruster Simulations,” *AIAA 2008-4924, 44th AIAA/ASME/SAE/ASEE Joint Propulsion Conference & Exhibit*, Hartford, CT, July 2008.
- ³¹Chesta, E., Meezan, N. B., and Cappelli, M. A., “Stability of a magnetized Hall plasma discharge,” *Journal of Applied Physics*, Vol. 89, No. 6, 2001, pp. 3099.
- ³²Fife, J., Martinez-Sanchez, M., and Szabo, J., “A Numerical Study of Low-Frequency Discharge Oscillations in Hall Thrusters,” *33rd AIAA/ASME/SAE/ASEE Joint Propulsion Conference & Exhibit*, Seattle, WA, 1997.
- ³³Boeuf, J. P. and Garrigues, L., “Low frequency oscillations in a stationary plasma thruster,” *Journal of Applied Physics*, Vol. 84, No. 7, 1998, pp. 3541.
- ³⁴Barral, S. and Ahedo, E., “Low-frequency model of breathing oscillations in Hall discharges,” *Physical Review E*, Vol. 79, No. 4, April 2009.
- ³⁵Barral, S. and Peradzynski, Z., “Ionization oscillations in Hall accelerators,” *Physics of Plasmas*, Vol. 17, No. 1, 2010.
- ³⁶Barral, S., Makowski, K., Peradzynski, Z., Gascon, N., and Dudeck, M., “Wall material effects in stationary plasma thrusters. II. Near-wall and in-wall conductivity,” *Physics of Plasmas*, Vol. 10, No. 10, 2003, pp. 4137.
- ³⁷Chen, F. F., *Introduction to plasma physics and controlled fusion.*, Plenum Press., New York, 1990.
- ³⁸Stix, T. H., *Waves in plasmas*, American Institute of Physics, New York, 1992.
- ³⁹Bellan, P. M., *Fundamentals of plasma physics*, Cambridge University Press, Cambridge, 2008.
- ⁴⁰Ellis, R. F., Marden-Marshall, E., and Majeski, R., “Collisional drift instability of a weakly ionized argon plasma,” *Plasma Physics*, Vol. 22, No. 2, Feb. 1980, pp. 113–131.
- ⁴¹Jorns, B. A. and Hofer, R. R., “Low Frequency Plasma Oscillations in a 6-kW Magnetically Shielded Hall Thruster,” American Institute of Aeronautics and Astronautics, July 2013.
- ⁴²Esipchuk, Y. and Tilinin, G. N., “Drift instability in a Hall-current plasma accelerator,” *Soviet Physics-Technical Physics*, Vol. 21, No. 4, April 1976.
- ⁴³Kapulkin, A. and Guelman, M. M., “Low-Frequency Instability in Near-Anode Region of Hall Thruster,” *IEEE Transactions on Plasma Science*, Vol. 36, No. 5, Oct. 2008, pp. 2082–2087.
- ⁴⁴Frias, W., Smolyakov, A. I., Kaganovich, I. D., and Raitsev, Y., “Long wavelength gradient drift instability in Hall plasma devices. I. Fluid theory,” *Physics of Plasmas*, Vol. 19, No. 7, 2012, pp. 072112.
- ⁴⁵Frias, W., Smolyakov, A. I., Kaganovich, I. D., and Raitsev, Y., “Long wavelength gradient drift instability in Hall plasma devices. II. Applications,” *Physics of Plasmas*, Vol. 20, No. 5, 2013, pp. 052108.
- ⁴⁶Ducrocq, A., Adam, J. C., Heron, A., and Laval, G., “High-frequency electron drift instability in the cross-field configuration of Hall thrusters,” *Physics of Plasmas*, Vol. 13, No. 10, 2006, pp. 102111.
- ⁴⁷Cavalier, J., Lemoine, N., Bonhomme, G., Tsikata, S., Honore, C., and Gresillon, D., “Hall thruster plasma fluctuations identified as the EB electron drift instability: Modeling and fitting on experimental data,” *Physics of Plasmas*, Vol. 20, No. 8, 2013, pp. 082107.
- ⁴⁸Lomas, P. J. and Kilkenny, J. D., “Electrothermal instabilities in a Hall accelerator,” *Plasma Physics*, Vol. 19, No. 4, April 1977, pp. 329–341.
- ⁴⁹Hara, K. and Boyd, I. D., “Low frequency oscillation analysis of a Hall Thruster using a one-dimensional hybrid-direct kinetic,” *IEPC-2013-266, 33rd International Electric Propulsion Conference*, Washington, D.C., Oct. 2013.
- ⁵⁰Hara, K., Boyd, I. D., and Kolobov, V. I., “One-dimensional hybrid-direct kinetic simulation of the discharge plasma in a Hall thruster,” *Physics of Plasmas*, Vol. 19, No. 11, 2012, pp. 113508.
- ⁵¹Barral, S. and Peradzynski, Z., “A new breath for the breathing mode,” *IEPC-2009-070, 31st International Electric Propulsion Conference*, Ann Arbor, MI, Sept. 2009.
- ⁵²King, L., “A (Re-)examination of Electron Motion in Hall Thruster Fields,” *IEPC-2005-258, 29th International Electric Propulsion Conference*, Princeton University, 2005.

Appendix

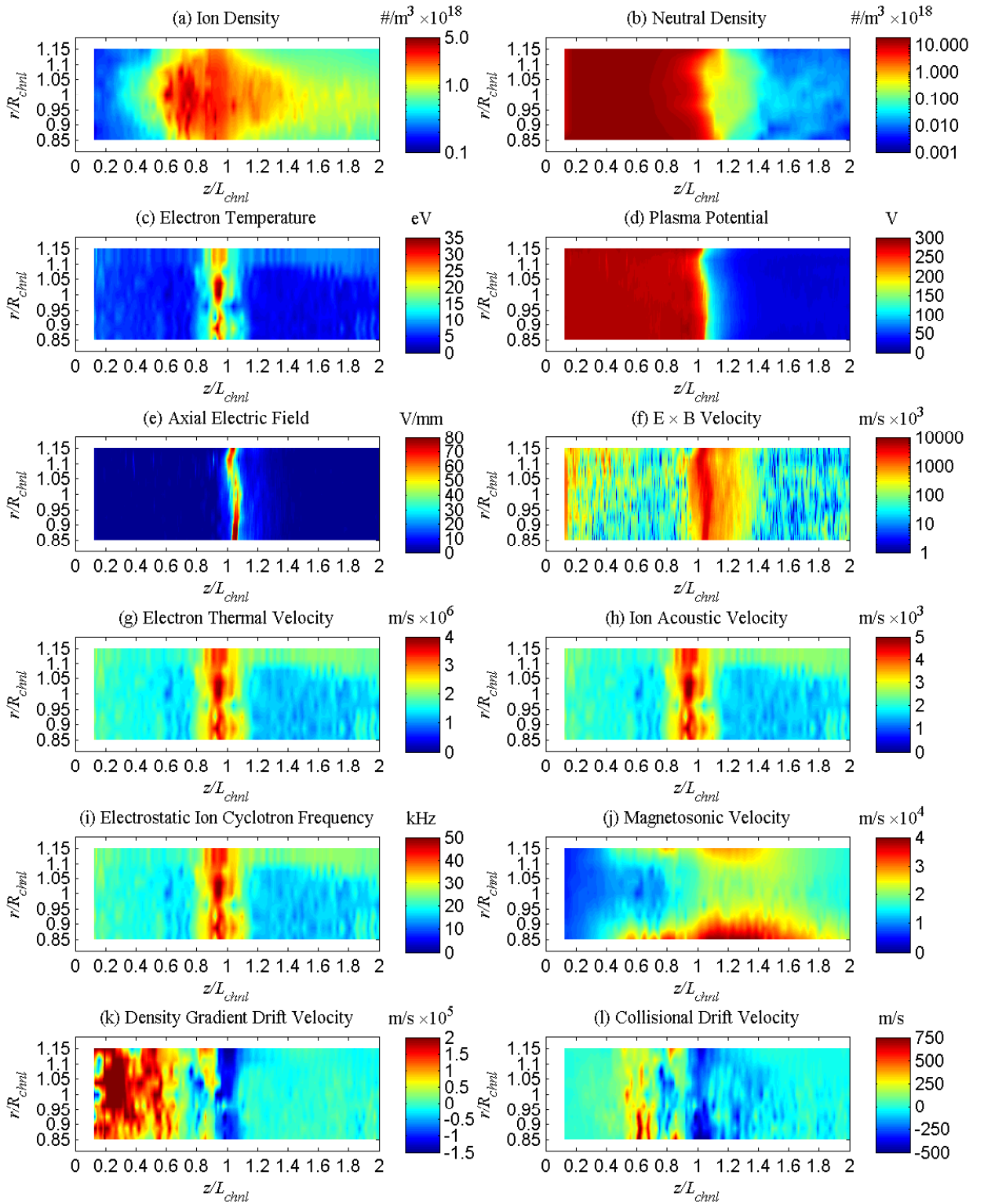


Figure 16: Internal measurements of the H6 discharge channel from Reid²⁵ as discussed in Table 1 for (a) ion density, (b) neutral density, (c) electron temperature (d) plasma potential, and (e) axial electric field. Calculated velocities include (f) $E \times B$ drift velocity, (g) electron thermal velocity, (h) ion acoustic velocity and (j) magnetosonic velocity, (k) density gradient drift velocity and (l) and collisional drift velocity. (i) is electrostatic ion cyclotron frequency.